

1    Size-resolved source apportionment of particulate matter  
2    in urban Beijing during haze and non-haze episodes

3    S. L Tian, Y. P. Pan, Y. S. Wang

4    *State Key Laboratory of Atmospheric Boundary Layer Physics and Atmospheric Chemistry*  
5    (*LAPC*), *Institute of Atmospheric Physics, Chinese Academy of Sciences, Beijing 100029, China*

6    \*Corresponding author. Tel.: +86 01082020530; fax: +86 01062362389.

7    E-mail address: wys@mail.iap.ac.cn (Y. Wang); panyuepeng@mail.iap.ac.cn (Y. Pan).

8

9    **Abstract:** Additional size-resolved chemical information is needed before the  
10    physicochemical characteristics and sources of airborne particles can be understood;  
11    however, this information remains unavailable in most regions of China due to  
12    lacking measurement data. In this study, we report observations of various chemical  
13    species in size-segregated particle samples that were collected over one year in the  
14    urban area of Beijing, a mega city that experiences severe haze episodes. In addition  
15    to fine particles, high concentrations of coarse particles were measured during the  
16    period of haze. The abundance and chemical compositions of the particles in this  
17    study were temporally and spatially variable, with major contributions from organic  
18    matter and secondary inorganic aerosols. The contributions of organic matter to the  
19    particle mass decreased from 37.9% to 31.2%, and the total contribution of sulfate,  
20    nitrate and ammonium ions increased from 19.1% to 33.9% between non-haze and  
21    haze days, respectively. Due to heterogeneous reactions and hygroscopic growth, the  
22    peak size distributions of the organic carbon, copper and sulfate, nitrate, ammonium,  
23    chloride, and potassium ions shifted from 0.43-0.65  $\mu\text{m}$  on non-haze days to 0.65-1.1  
24     $\mu\text{m}$  on haze days. Although the size distributions of lead, cadmium and thallium were  
25    similar during the observation period, their concentrations increased by a factor of  
26    more than 1.5 on haze days compared with non-haze days. We observed that  
27    ammonium, which has a size range of 0.43-0.65  $\mu\text{m}$ , sulfate and nitrate, which have a  
28    size range of 0.65-1.1  $\mu\text{m}$ , calcium ions, which have a size range of 5.8-9  $\mu\text{m}$ , and the  
29    meteorological factors of relative humidity and wind speed were responsible for haze  
30    pollution when the visibility was less than 10 km. Source apportionment using

positive matrix factorization showed six  $PM_{2.1}$  sources and seven  $PM_{2.1-9}$  common sources: secondary inorganic aerosol (25.1% for fine particles vs. 9.8% for coarse particles), coal combustion (17.7% vs. 7.8%), biomass burning (11.1% vs. 11.8%), industrial pollution (12.1% vs. 5.1%), road dust (8.4% vs. 10.9%), vehicle emissions (19.6% for fine particles), mineral dust (22.6% for coarse particles) and organic aerosol (23.6% for coarse particles). The first four factors and vehicle emissions were higher on haze days, while the contributions of road dust and mineral dust were higher on non-haze days. The sources generally increased as the size decreased, with the exception of mineral dust. However, two peaks were consistently found in the fine and coarse particles. In addition, the contributing sources varied with the wind direction, with coal and oil combustion products increasing during southern flows. This result suggests that future air pollution control strategies should consider wind patterns, especially during episodes of haze. Furthermore, the findings of this study indicated that the  $PM_{2.5}$ -based dataset is insufficient for determining source control policies for haze in China and that detailed size-resolved information is needed to characterize the important sources of particulate matter in urban regions and better understand severe haze pollution.

**Keywords:** Source apportionment; Size distribution; Haze episodes; Particulate matter; Beijing

## 50 **Introduction**

Particulate matter (PM) is among the most important atmospheric pollutants that negatively affect human health and visibility. In addition, PM plays a significant role in global climate change through its direct and indirect affects and ecosystem cycling (Huang et al., 2014; McFiggans, 2014; Pan et al., 2013). Due to rapid industrialization and urbanization in recent decades, China has become one of the most significant source regions for anthropogenic atmospheric emissions in the world (Guo et al., 2014). The Chinese capital of Beijing, a megacity with approximately 21 million inhabitants (Beijing statistical yearbook 2013), is experiencing extreme haze events

59 (Sun et al., 2006). From November 30 to December 2 and December 7 to December 8,  
60 2004, the highest concentration of  $\text{PM}_{2.5}$  (particulate matter with aerodynamic  
61 diameter lower than  $2.5 \mu\text{m}$ ) over 6 hours was  $329.8 \mu\text{g m}^{-3}$  (Sun et al., 2006). During  
62 the haze episode in January 2013, the highest instantaneous five-minute  $\text{PM}_{2.5}$   
63 concentration was  $770 \mu\text{g m}^{-3}$  at 20:48 on January 12, 2013 (Tian et al., 2014).  
64 Moreover, the highest instantaneous  $\text{PM}_{2.5}$  concentration reached  $1000 \mu\text{g m}^{-3}$  in  
65 some heavily polluted areas of Beijing (Quan et al., 2014). Although previous studies  
66 have provided valuable information regarding the physical and chemical  
67 characteristics of PM in urban Beijing and its surrounding areas (Li et al., 2013; Du et  
68 al., 2014; Song et al., 2006; Chan et al., 2005; Schleicher et al., 2013; Sun et al., 2004),  
69 the factors that influence haze formation remain unclear due to its complexity (Yang  
70 et al., 2014; Jing et al., 2014). In addition, previous studies have primarily focused on  
71 single particle fractions, such as  $\text{PM}_{2.5}$ , and have neglected size-resolved chemical  
72 information, especially for coarse particles, which also play an important role in haze  
73 events (Tian et al., 2014; Sun et al., 2013).

74 Knowing the size distributions and associated chemical species is crucial for  
75 evaluating the effects of PM on human health, visibility, and regional radiative  
76 forcing, and for determining the sources, formation mechanisms and conversion  
77 processes of the particles (Pillai and Moorthy, 2001; Duarte et al., 2008; Liu et al.,  
78 2008; Contini et al., 2014). Typically, mass distribution of PM is dominated by three  
79 modes (or sub-modes): the condensation ( $\sim 0.1\text{--}0.5 \mu\text{m}$ ), droplet ( $\sim 0.5\text{--}2 \mu\text{m}$ ) and  
80 coarse ( $> 2 \mu\text{m}$ ) modes (Wang et al., 2012; Guo et al., 2010). Thus, to simplify mass  
81 distribution calculations in this study, the particle modes were divided. The sizes of  
82 the condensation mode particles were between  $0.43$  and  $0.65 \mu\text{m}$ , and the sizes of the  
83 droplet-mode particles were between  $0.65$  and  $2.1 \mu\text{m}$ . Recent results have suggested  
84 that secondary sulfates and nitrates primarily form fine particles, with elevated  
85 concentrations in the droplet mode during haze days (Sun et al., 2013; Wang et al.,  
86 2012). During the extreme haze events in urban Beijing in early 2013, the peak mass

87 concentration of particles shifted from 0.43-0.65  $\mu\text{m}$  on clear days to 0.65-1.1  $\mu\text{m}$  on  
88 lightly polluted days and 1.1-2.1  $\mu\text{m}$  on heavily polluted days due to the hygroscopic  
89 growth of submicron particles and the formation of secondary particles, including  
90 organic carbon (OC) and sulfate ( $\text{SO}_4^{2-}$ ), nitrate ( $\text{NO}_3^-$ ) and ammonium ( $\text{NH}_4^+$ ) ions  
91 (Tian et al., 2014). Because long-term observations are lacking, it is unclear whether  
92 the peak shifts occurred during other periods or whether this phenomenon only  
93 occurred during the extreme haze events in early 2013.

94 In addition, source apportionment based on size-fractionated PM data would  
95 provide additional insights regarding aerosol sources, especially during haze events  
96 (Pant and Harrison, 2012). For example, receptor models have been successfully used  
97 to identify coarse aerosol sources separately of fine aerosol sources (Karanasiou et al.,  
98 2009; Titos et al., 2014). Source apportionment studies have shown that the sources of  
99 PM<sub>10</sub> (particulate matter with aerodynamic diameter lower than 10  $\mu\text{m}$ ) and PM<sub>2.5</sub> are  
100 different. Meanwhile, the features of sources and dominant sources during different  
101 periods are different (Karanasiou et al., 2009; Vecchi et al., 2008), and understanding  
102 the sources of size-resolved chemical species (i.e., OC,  $\text{SO}_4^{2-}$ ,  $\text{NO}_3^-$  and  $\text{NH}_4^+$ ) is  
103 important for strategy-makers to effectively control and manage pollution (Hou et al.,  
104 2011; Zhang et al., 2014a; Fisher et al., 2011).

105 The main source apportionment methods can be divided into three categories:  
106 emissions inventory, diffusion model and receptor model. Among these categories,  
107 receptor models have been widely used because the methods are not limited by  
108 pollution discharge conditions, weather or terrain factors. The receptor models based  
109 on chemical analysis can be divided into two categories: one in which source profiles  
110 are needed, such as the Chemical Mass Balance (CMB) method; and one in which  
111 source profiles are not needed, such as the Positive Matrix Factorization (PMF)  
112 method. Because it is difficult to build large and accurate source profiles, we use the  
113 PMF method to perform source apportionment in our study. Previously, source  
114 apportionment studies in Beijing have mainly focused on single size fractions (i.e.,

115  $\text{PM}_{2.5}$ ,  $\text{PM}_{10}$ ). Overall, the results showed that the contributions of major sources to  
116  $\text{PM}_{2.5}$  mass in Beijing exhibited seasonal and annual variations. The major sources of  
117  $\text{PM}_{2.5}$  mass in Beijing during 2000 were dust (20%), secondary sulfate (17%),  
118 secondary nitrate (10%), coal combustion (7%), diesel and gasoline exhaust (7%),  
119 secondary ammonium (6%), biomass aerosol (6%), cigarette smoke (1%), and  
120 vegetative detritus (1%) (Zheng et al., 2005). However, the PMF model identified six  
121 main sources of  $\text{PM}_{2.5}$  in 2009-2010: soil dust, coal combustion, biomass burning,  
122 traffic and waste incineration emissions, industrial pollution, and secondary inorganic  
123 aerosols, with annual mean contributions of 16, 14, 13, 3, 28, and 26%, respectively,  
124 (Zhang et al., 2013b). In addition, the PMF method resolved 87 and 80% of the  $\text{PM}_{2.5}$   
125 in January and August 2004, respectively. The major sources were coal combustion  
126 (38% in January and 11% August), secondary sulfate (9% and 24%), secondary  
127 nitrate (10% and 8%), biomass burning (15% and 1%), motor vehicle emissions (8%  
128 and 15%) and road dust (7% and 8%) (Song et al., 2007). Previous studies regarding  
129 the size distributions of PM in urban Beijing have primarily focused on limited  
130 chemical species (Sun et al., 2013; Li et al., 2013; Yao et al., 2003) or have been  
131 conducted over short periods (Li et al., 2012; Sun et al., 2010; Gao et al., 2012; Zhang  
132 et al., 2014b). To the best of our knowledge, no studies have been conducted on the  
133 source apportionment of size-resolved atmospheric particles based on long-term  
134 observations in urban Beijing.

135 To fill this knowledge gap, we observed size-resolved PM in urban Beijing from  
136 March 1, 2013 to February 28, 2014. In this study, we report the mass closure of  
137 particles based on a size-resolved chemical dataset obtained from haze and non-haze  
138 days over four seasons. The PMF method was combined with back trajectory cluster  
139 analysis to estimate the relative contributions of sources in different size fractions  
140 between haze and non-haze days and among different regional sources. These results  
141 will help policy-makers design emission control strategies and can serve as a database  
142 for future field measurements and modeling studies.

143 **2. Materials and Methods**

144 **2.1. Sampling site**

145 The experiment was performed from March 1, 2013, to February 28, 2014, at the  
146 Institute of Atmospheric Physics, Chinese Academy of Sciences (39°58'N, 116°22'E)  
147 (Fig. S1). The samplers were placed on the roof of a building approximately 15 m  
148 above the ground. The sampling site was located in Northwest Beijing between the  
149 3rd and 4th ring roads. The site was selected to broadly represent the air pollution  
150 levels in urban Beijing because it was far from specific point emission sources.

151 **2.2. Sampling collection**

152 Two 9-stage samplers (Andersen Series 20-800, USA) with cutoff points of 0.43,  
153 0.65, 1.1, 2.1, 3.3, 4.7, 5.8, and 9.0  $\mu\text{m}$ , were used to simultaneously collect particles  
154 for 48 h (from 10:00 (local time, LT) on Monday to 10:00 LT on Wednesday) every  
155 week at a flow rate of 28.3  $\text{L min}^{-1}$ . Overall, 52 sets of size-resolved PM samples were  
156 collected on quartz fiber filters and cellulose membranes (81 mm in diameter) during  
157 the study period. The quartz fiber filters were pre-fired (2 h at 800 °C) to remove all  
158 organic material and were weighed before and after sampling using a microbalance  
159 with a sensitivity of  $\pm 0.01$  mg. Filters were conditioned in a dryer at  $25 \pm 3$  °C under a  
160 relative humidity (RH) of  $22 \pm 3\%$  for 72 h before each weighing. After re-weighing,  
161 the exposed filters were stored in a freezer at  $-20$  °C to limit losses of volatile  
162 components loaded on the filters. To prevent the sampler from becoming blocked by  
163 particles during sampling, the samplers were cleaned using an ultrasonic bath for 30  
164 min before each sampling. In addition, the sampling flow rates were calibrated before  
165 each sample was collected and were monitored using a flow meter during each  
166 sampling. Field blanks (a blank quartz filter and a blank cellulose membrane in each  
167 sampling) were used to determine any possible background contamination. All of the  
168 tools used during sampling and analysis were cleaned, and the operator wore plastic  
169 gloves. Meanwhile, the meteorological parameters used in this study, including  
170 visibility, temperature, RH, wind speed (WS) and wind direction (WD), were

171 collected at Beijing Capital International Airport (<http://english.wunderground.com>)  
172 (Fig. S2).

173 **2.3 Chemistry analyses**

174 A quarter of each quartz filter was subjected to extraction in 25 ml of deionized  
175 water (Millipore, 18.2 MΩ) in an ultrasonic bath for 30 min. The extraction liquid was  
176 filtered and subsequently measured using ion chromatography (DIONEX, ICS-90,  
177 USA) to determine the sodium ( $\text{Na}^+$ ),  $\text{NH}_4^+$ , potassium ( $\text{K}^+$ ), magnesium ( $\text{Mg}^{2+}$ ),  
178 calcium ( $\text{Ca}^{2+}$ ), chloride ( $\text{Cl}^-$ ),  $\text{NO}_3^-$  and  $\text{SO}_4^{2-}$  ion concentrations. For ion analysis,  
179 the **ion chromatography** was equipped with a separation column (Ionpac CS12A  
180 4×250 mm for cations and Ionpac AS14A 4×250 mm for anions) and a suppressor  
181 (CSRS300–4 mm for cations and ASRS 300–4 mm for anions). The eluents used for  
182 cations and anions were 22 mmol L<sup>-1</sup> MSA and 3.5 mmol L<sup>-1</sup>  $\text{Na}_2\text{CO}_3$ /1 mmol L<sup>-1</sup>  
183  $\text{NaHCO}_3$ , respectively. The ions were quantified by external standard curves every  
184 week, and one trace calibration standard solution was used to check the curve each  
185 day. The limit of detection was less than 0.02  $\mu\text{g m}^{-3}$  for all ions when the injection  
186 volume was 100  $\mu\text{L}$ .

187 Using another quarter of each quartz filter, the concentrations of OC and  
188 elemental carbon (EC) were determined using a thermal/optical carbon aerosol  
189 analyzer (DRI Model 2001A, Desert Research Institute, USA). Briefly, a punch  
190 aliquot (0.495 cm<sup>2</sup>) of a quartz fiber filter sample was heated stepwise in an oven at  
191 140 °C (OC1), 280 °C (OC2), 480 °C (OC3) and 580 °C (OC4) under a pure helium  
192 atmosphere to volatilize the OC before heating to 580 °C (EC1), 740 °C (EC2) and  
193 840 °C (EC3) in a 2% oxygen-contained helium atmosphere for EC oxidation. At each  
194 stage, the formed  $\text{CO}_2$  was catalytically converted to  $\text{CH}_4$  by a  $\text{MnO}_2$  catalyst, and the  
195 resulting  $\text{CH}_4$  was measured using a flame ionization detector. The analyzer was  
196 calibrated before and after sample analysis by using a standard mixture of  $\text{CH}_4$  and  
197  $\text{CO}_2$ . One sample was randomly selected from every 10 samples to conduct duplicate  
198 sample analyses. The measurement errors were less than 10% for TC (OC+EC), and

199 the OC and EC concentrations in the field blanks were less than 1% of the sample  
200 levels and were subtracted from the samples.

201 A quarter of the cellulose membrane was digested in a mixture of concentrated  
202  $\text{HNO}_3$  (6 ml),  $\text{HCl}$  (2 ml) and  $\text{HF}$  (0.2 ml) in a closed vessel microwave digestion  
203 system (MARS5, CEM Corporation, Matthews, NC, USA). Then, an Agilent 7500a  
204 inductively coupled plasma mass spectrometer (ICP-MS, Agilent Technologies,  
205 Tokyo, Japan) was used to determine the concentrations of 21 trace elements (TEs)  
206 (sodium (Na), magnesium (Mg), Aluminum (Al), potassium (K), Calcium (Ca),  
207 Manganese (Mn), Iron (Fe), cobalt (Co), Nickel (Ni), Copper (Cu), Zinc (Zn),  
208 molybdenum (Mo), cadmium (Cd), Barium (Ba), thallium (Tl), Lead (Pb), thorium  
209 (Th) and uranium(U)). A blank filter was analyzed in each batch for quality control.  
210 Quantitative analysis was conducted using external calibration standards with  
211 concentrations that were similar to those in the samples. In addition, internal standard  
212 elements ( $^{45}\text{Sc}$ ,  $^{72}\text{Ge}$ ,  $^{115}\text{In}$  and  $^{209}\text{Bi}$ ) were added online during the metallic element  
213 analysis.

214 The analysis methods, information regarding the instruments used in this study  
215 (e.g., precision, calibration and detection limit) and quality control methods are  
216 described elsewhere (Pan and Wang, 2015; Li et al., 2012).

217 **2.4 Chemical mass closure**

218 Mass closure was used to discuss the relative contributions of the major  
219 components in the PM. The chemical species were divided into the following seven  
220 categories: sulfate-nitrate-ammonium (SNA), **organic matter (OM)**, crustal materials  
221 (CM), heavy metals (HM), EC, sea salt (SS) and liquid water (LW). The difference  
222 between the mass weighted by microbalance and that reconstructed using the above  
223 seven components was defined as unidentified matter (UM). The calculation methods  
224 of the main components were described in our previous studies (Tian et al., 2014) and  
225 are shown in Table S1 for convenience.

226 **2.5 PMF model**

227 PMF is an effective source apportionment receptor model (Karanasiou et al., 2009;  
228 Bullock et al., 2008; Paatero and Tapper, 1994; Paatero, 1997). In this study,  
229 EPA-PMF 3.0 was applied separately for the fine (the input data included the mass  
230 concentrations and chemical species in the particles with sizes of < 0.43, 0.43-0.65,  
231 0.65-1.1 and 1.1-2.1  $\mu\text{m}$ ) and coarse (the input data included the mass concentrations  
232 and chemical species for particles with sizes of 2.1-3.3, 3.3-4.7, 4.7-5.8 and 5.8-9  $\mu\text{m}$ )  
233 fractions. Both the numbers of samples analyzed for the fine and coarse fractions were  
234 208. The chemical species included Na, Mg, Al, K, Ca, Mn, Fe, Co, Ni, Cu, Zn, Mo,  
235 Cd, Ba, Tl, Pb, Th, U,  $\text{Na}^+$ ,  $\text{NH}_4^+$ ,  $\text{K}^+$ ,  $\text{Mg}^{2+}$ ,  $\text{Ca}^{2+}$ ,  $\text{Cl}^-$ ,  $\text{SO}_4^{2-}$ ,  $\text{NO}_3^-$ , OC and EC. The  
236 uncertainty of the concentration data, which was also the input data, was calculated as  
237 shown below.

238 If the concentration is less than or equal to the provided method detection limit  
239 (MDL), the uncertainty is calculated using the following equation:

240 
$$\text{Uncertainty} = 5/6 \times \text{MDL} \quad (1)$$

241 If the concentration is greater than the provided MDL, the calculation is

242 
$$\text{Uncertainty} = \sqrt{(\text{Error Fraction} \times \text{concentration})^2 + (\text{MDL})^2} \quad (2)$$

243 In this study, the error fraction was estimated as 10 (the percent uncertainty  
244 multiplied by 100) for all of the chemical species, and the MDLs were similar to those  
245 reported in previous studies (Li et al., 2012; Yang et al., 2009).

246 The base model was run 20 times with a different number of factors to obtain the  
247 best possible solution. During the first run, several species had a large number of  
248 absolute scaled residuals greater than 3, which indicated poor observed-predicted  
249 correlations. Then, these species were designated as “weak” and the model was rerun.  
250 When a reasonable solution was found, the bootstrapping technique was used to  
251 obtain the most meaningful results. Overall, 100 bootstrap runs were performed with a  
252 minimum  $r^2$ -value of 0.6. Of the 100 runs, the factors were mainly mapped to a base  
253 factor in every run, which indicated a stable result.

254 Several criteria are important for ensuring a good PMF solution. First, the  
255 modeled Q's should be within 50% of the theoretical value. Second, the optimum  
256 number of factors should be determined by the criterion that each factor has a  
257 distinctively dominant grouping of compounds. Third, the model uncertainty  
258 produced by bootstrapping should be small. The principles are detailed elsewhere (Liu  
259 et al.; Titos et al., 2014; Moon et al., 2008).

## 260 **2.6 Air mass back trajectory cluster**

261 The three-day backward trajectories arriving at the sampling site were calculated  
262 using the National Oceanic and Atmospheric Administration (NOAA) HYSPLIT 4  
263 model with a  $0.5^{\circ} \times 0.5^{\circ}$  latitude-longitude grid. The arrival level was set at 500 m  
264 above ground level (a.g.l.). The HYSPLIT model was run four times each day at  
265 starting times of 02:00, 08:00, 14:00, and 20:00 UTC during the sampling period.  
266 Then, all of the trajectories were divided into different groups based on the horizontal  
267 moving speed and direction of the air masses to form the trajectory clusters (Sirois  
268 and Bottenheim, 1995; Wang et al., 2006b).

## 269 **3. Results**

### 270 **3.1 PM mass concentrations and chemical composition**

271 Table 1 describes the concentrations of the size-resolved mass and chemical  
272 compositions during different seasons. The annual average concentrations of  $\text{PM}_{2.1}$   
273 (particulate matter with aerodynamic diameters less than  $2.1 \mu\text{m}$ ) and  $\text{PM}_9$  (particulate  
274 matter with aerodynamic diameters less than  $9 \mu\text{m}$ ) were  $67.3$  and  $129.6 \mu\text{g m}^{-3}$ ,  
275 respectively. Although the present level of  $\text{PM}_{2.1}$  is significantly lower than that in  
276 2009-2010 ( $135 \mu\text{g m}^{-3}$ ) (Zhang et al., 2013b), it was more than times higher than the  
277 National Ambient Air Quality Standard (NAAQS), which specifies an annual average  
278  $\text{PM}_{2.5}$  of  $15 \mu\text{g m}^{-3}$  (GB3095-2012, Grade I). In addition,  $\text{PM}_9$  was approximately  
279 three times the NAAQS annual average  $\text{PM}_{10}$  of  $40 \mu\text{g m}^{-3}$  (Grade I). Thus, fine and  
280 coarse particles, defined in this study as particles with sizes  $< 2.1$  ( $\text{PM}_{2.1}$ ) and  $2.1\text{-}9.0$   
281  $\mu\text{m}$  ( $\text{PM}_{2.1\text{-}9}$ ), respectively, are important for PM in urban Beijing.

282 As shown in Table 1, the primary components of  $\text{PM}_{2.1}$  are OC (24.5% of  $\text{PM}_{2.1}$ ),  
283  $\text{SO}_4^{2-}$  (14.7%),  $\text{NO}_3^-$  (11.2%) and  $\text{NH}_4^+$  (9.2%). In contrast, Ca ( $3.5 \pm 1.5 \text{ } \mu\text{g m}^{-3}$ ), EC  
284 ( $2.0 \pm 1.8 \text{ } \mu\text{g m}^{-3}$ ) and other species accounted for approximately 40% of  $\text{PM}_{2.1}$ . The  
285 composition of the coarse particles was different from the composition the fine  
286 particles ( $\text{PM}_{2.1}$ ). In this study the highest contribution to  $\text{PM}_{2.1-9}$  was Ca (16.3% of  
287  $\text{PM}_{2.1-9}$ ), followed by OC (15.5%),  $\text{NO}_3^-$  (4.5%), Fe (4.1%) and  $\text{SO}_4^{2-}$  (3.5%). These  
288 species accounted for approximately 44% of  $\text{PM}_{2.1-9}$ . The mass closure of  
289 size-resolved particles is discussed in detail below (Sect. 4.2).

### 290 3.2 Seasonality

291 The concentrations of  $\text{PM}_{2.1}$  were greatest during winter (December to February,  
292  $76.8 \text{ } \mu\text{g m}^{-3}$ ), followed by spring (March to May), summer (June to August) and  
293 autumn (September to November), with concentrations of approximately  $65 \text{ } \mu\text{g m}^{-3}$   
294 during the latter three seasons (Table 1). In contrast, the concentrations of  $\text{PM}_{2.1-9}$   
295 decreased in the following order spring > autumn > winter > summer.

296 The seasonal dependency varied with species. For most of the species that were  
297 enriched in the fine mode (with a  $\text{PM}_{2.1}/\text{PM}_9$  chemical concentration ratio greater than  
298 0.5, including  $\text{NH}_4^+$ , Tl, Cd, Pb,  $\text{SO}_4^{2-}$ ,  $\text{NO}_3^-$ , EC,  $\text{K}^+$ , Zn,  $\text{Cl}^-$ , OC, Cu, Na,  $\text{Na}^+$ , Mo  
299 and K), in the compositions of  $\text{PM}_{2.1}$  and  $\text{PM}_{2.1-9}$  exhibited similar seasonal variations,  
300 with the  $\text{PM}_{2.1}$  mass concentration being higher during colder seasons. However, the  
301 seasonal dependence of the concentration of certain species in  $\text{PM}_{2.1}$  differs from the  
302 typical seasonal variation. For example, the concentrations of  $\text{SO}_4^{2-}$  and  $\text{NH}_4^+$  in  
303 spring and summer were higher than those in autumn and winter. This result was  
304 consistent with the seasonal variability of  $\text{SO}_4^{2-}$  and  $\text{NH}_4^+$  in  $\text{PM}_{2.5}$  in 2009-2010  
305 (Zhang et al., 2013b).

306 In addition, the OC concentrations in  $\text{PM}_{2.1}$  decreased as follows: summer ( $20.2 \text{ } \mu\text{g m}^{-3}$ ) >  
307 spring ( $16.5 \text{ } \mu\text{g m}^{-3}$ ) > winter ( $16.2 \text{ } \mu\text{g m}^{-3}$ ) > autumn ( $13.4 \text{ } \mu\text{g m}^{-3}$ ). The  
308 high OC concentrations during the summer primarily resulted from the photochemical  
309 generation of more secondary organic carbon (SOC). This result can be confirmed by

310 the OC/EC ratios, which exhibited the following seasonal pattern: summer (16.7) >  
311 spring (12.7) > autumn (6.7) > winter (4.9). Because EC primarily arises from  
312 primary combustion emissions, the OC/EC ratios were used to evaluate the  
313 contributions from secondary organic carbon (Cao et al., 2007).

314 For species enriched in the coarse mode (PM<sub>2.1-9</sub>) (with a PM<sub>2.1</sub>/PM<sub>9</sub> chemical  
315 concentration ratio below 0.5, including Ni, Mn, U, Co, Mg<sup>2+</sup>, Th, Al, Ba, Mg, Ca and  
316 Ca<sup>2+</sup>), their PM<sub>2.1</sub> and PM<sub>2.1-9</sub> concentrations demonstrated typical seasonal variations,  
317 with higher concentrations observed during the spring and autumn (or winter) due to  
318 the influences of re-suspended soil dust. Re-suspended soil dust may result from both  
319 long transport dust and local anthropogenic sources (construction dust and mechanical  
320 abrasion processes). The relatively high wind speed during spring facilitated the  
321 ascent of road dust into the atmosphere and resulted in the relatively high value of the  
322 species in the coarse mode (Liu et al., 2014a).

### 323 **3.3 Size distribution**

324 The size distributions of the mass concentrations and the chemical species are  
325 shown in Fig. 1 and Fig. S3. In each season, the size distribution of the mass  
326 concentrations was bimodal. The fine modes commonly showed maxima at 0.65-1.1  
327  $\mu\text{m}$  in spring, autumn and winter and 0.43-0.65  $\mu\text{m}$  in summer. The coarse modes  
328 showed maxima at 4.7-5.8  $\mu\text{m}$  in all of the seasons. As shown in Fig. 1, the peak of  
329 the fine mode was broader in winter than in the other seasons, indicating the  
330 complexity of the emissions in winter (Sun et al., 2013). Emissions from coal  
331 combustion for heating are greater during winter, especially for retail coal combustion  
332 in surrounding areas, which is difficult to control (Wang et al., 2006a). However, the  
333 meteorological conditions in winter are unfavorable for the diffusion of fine particles  
334 and precursors (SO<sub>2</sub>, NO<sub>x</sub>, VOCs), making secondary particle emissions more  
335 complex.

336 The chemical species can generally be divided into three groups based on their  
337 size distributions. First, SO<sub>4</sub><sup>2-</sup>, NO<sub>3</sub><sup>-</sup>, NH<sub>4</sub><sup>+</sup>, EC, Zn, Cd, Pb and Tl were abundant in

338 the fine mode, which exhibited maxima at 0.43-0.65  $\mu\text{m}$  or 0.65-1.1  $\mu\text{m}$  in all four  
339 seasons that corresponded to coal and motor vehicle sources (Li et al., 2013). Second,  
340  $\text{Ca}^{2+}$ ,  $\text{Mg}^{2+}$ ,  $\text{Ba}$ ,  $\text{Mg}$ ,  $\text{Al}$ ,  $\text{Ca}$ ,  $\text{Fe}$ ,  $\text{Co}$ ,  $\text{Ni}$ ,  $\text{Th}$  and  $\text{U}$  were primarily concentrated in the  
341 coarse mode from 4.7 to 5.8  $\mu\text{m}$ , which suggested natural sources from soil dust or  
342 mechanical abrasion processes (Sun et al., 2013; Maenhaut et al., 2002). Third,  $\text{OC}$ ,  
343  $\text{Cl}^-$ ,  $\text{K}^+$ ,  $\text{Na}^+$ ,  $\text{Na}$ ,  $\text{K}$ ,  $\text{Mn}$ ,  $\text{Cu}$  and  $\text{Mo}$  exhibited typical bimodal distributions, and the  
344 amplitude of the fine mode was well correlated with that of the coarse mode. These  
345 species exhibited maxima at 0.43-0.65  $\mu\text{m}$  or 0.65-1.1  $\mu\text{m}$  and peaked at 4.7-5.8  $\mu\text{m}$  in  
346 the coarse mode.  $\text{Cl}^-$  and  $\text{K}^+$  are good biomass burning tracers (Du et al., 2011), and  
347  $\text{Mn}$  and  $\text{Cu}$  are good industrial pollution tracers. Hence, the species in the third group  
348 may represent mixed sources from biomass burning and industrial pollution.

349 The size distribution of the mass concentration and  $\text{OC}$  peaked at 0.43-0.65  $\mu\text{m}$  in  
350 summer and 0.65-1.1  $\mu\text{m}$  in winter. Because the primary organic carbon emissions  
351 were relatively stable across the four seasons, the size distribution differences in the  
352 fine mode primarily resulted from the generation of  $\text{SOC}$  (Duan et al., 2005). The  
353 difference between summer and winter indicated that the  $\text{SOC}$  formation in summer  
354 was enhanced due to photochemical reactions and primarily accumulated in  
355 “condensation mode” (Zhang et al., 2008). However, because photochemistry is  
356 typically weak in winter, the  $\text{SOC}$  generation mainly resulted from the high RH and  
357 high precursor concentrations, including volatile organic compounds (VOCs) from  
358 biological and anthropogenic sources (Jacobson et al., 2000). Thus, VOCs primarily  
359 accumulated in “droplet mode” (Cao et al., 2007). Previously, our findings indicated  
360 that weakening incident solar radiation reduces the formation of  $\text{SOC}$  formation in the  
361 smaller size fraction and that high RH plays an important role in the generation of  
362  $\text{SOC}$  in larger size fractions (Tian et al., 2014).

### 363 **3.4 Ion balance**

364 We calculated the ion balance for each size fraction, which was used to evaluate  
365 the ion deficiency between cations and anions in the PM (Fig. S4). The average

366 equivalent ratio of total cations ( $\text{Na}^+$ ,  $\text{NH}_4^+$ ,  $\text{K}^+$ ,  $\text{Mg}^{2+}$ , and  $\text{Ca}^{2+}$ ) to total anions ( $\text{SO}_4^{2-}$ ,  
367  $\text{NO}_3^-$  and  $\text{Cl}^-$ ) ranged from 0.95 to 2.50, with lowest ratio occurring in the 1.1-2.1  $\mu\text{m}$   
368 size fraction and highest ratio occurring in the 4.7-5.8  $\mu\text{m}$  size fraction. The total  
369 cation to total anion ratio in the fine particles was near unity throughout the year,  
370 which indicated excellent charge balance and high data quality. The slope for the fine  
371 mode particles was mainly greater than 1 because the concentrations of  $\text{CO}_3^{2-}$  and  
372  $\text{HCO}_3^-$  were not determined.

373 Fig. S5 shows good correlations between the  $\text{NH}_4^+$  and  $\text{SO}_4^{2-}$  concentrations in  
374 the fine particles for the data sets in different seasons, with  $\text{NH}_4^+/\text{SO}_4^{2-}$  equivalent  
375 ratios greater than 1 (spring (1.92) summer (1.79), autumn (1.01), winter (1.36)),  
376 revealing the dominance of  $(\text{NH}_4)_2\text{SO}_4$ . Next, we calculated the molar ratio of  $\text{NH}_4^+$  to  
377  $[\text{NO}_3^- + \text{SO}_4^{2-}]$ , which was slightly higher than unity in spring (1.25) and summer  
378 (1.33) and indicated the presence of  $\text{NH}_4\text{NO}_3$  in the fine aerosols. However, the ratios  
379 were less than one in the autumn (0.78) and winter (0.68), which indicated that  $\text{NO}_3^-$   
380 could be present in chemical forms other than  $\text{NH}_4\text{NO}_3$ .

381 For the coarse mode particles, the  $\text{NH}_4^+/\text{SO}_4^{2-}$  equivalent ratios in spring (0.78)  
382 summer (0.68) and autumn (0.58) were less than 1 but greater than 0.5, which  
383 indicated the dominance of  $(\text{NH}_4)_2\text{SO}_4$  and  $\text{NH}_4\text{HSO}_4$ . By contrast, the ratio in winter  
384 (1.33) was greater than unity, and the equivalent ratio of  $\text{NH}_4^+$  to  $[\text{NO}_3^- + \text{SO}_4^{2-}]$  in  
385 winter was less than unity.

## 386 4. Discussion

### 387 4.1 Size-resolved aerosol compositions on non-haze and haze days

388 Fig. 2 illustrates the size-segregated PM mass concentrations during the sampling  
389 period. Haze is defined as a weather phenomenon in which a high concentration of  
390 fine particles occur that result in a visibility of less than 10 km at a relative humidity  
391 (RH) of less than 90% (Sun et al., 2006; Tan et al., 2009; Zhuang et al., 2014). Thus,  
392 we used visibility and RH to determine the haze/no-haze days as follows: sampling  
393 days with visibility < 10 km and RH < 90% were defined as haze days and sampling

394 days with visibility > 10 km and RH < 90% were defined as non-haze days. During  
395 the observation period, 12 sets of size-resolved PM samples were collected during  
396 non-haze days and 19 sets were collected during haze days (marked in Fig. 2). Of the  
397 remaining 21 sets, 15 sets were collected during rain, snow or fog days and 6 sets  
398 were collected during dust days (visibility < 10 km, RH < 40%). These samples were  
399 excluded from the dataset when we discussed the differences between haze and  
400 non-haze days.

#### 401 **4.1.1 Concentration enhancement ratios**

402 Table S2 describes the annual average concentrations of the size-resolved mass  
403 and chemical compositions on haze and non-haze days over four seasons. The annual  
404 average  $PM_{2.1}$  and  $PM_{2.1-9}$  concentrations on haze days were 86.1 and 72.6  $\mu\text{g m}^{-3}$ ,  
405 which were 2.6 and 1.4 times those on non-haze days, respectively. Therefore, it is  
406 evident that fine particles significantly accumulated during the haze pollution period  
407 (Wang et al., 2014). In addition, the mass concentration enhancement ratio from  
408 non-haze to haze days ( $R_{H/N}$ ) was examined during all four seasons.

409 
$$R_{H/N} = C_H/C_N, \quad (3)$$

410  $C_H$ —Concentration of chemical species on haze days;

411  $C_N$ —Concentration of chemical species on non-haze days.

412 The  $R_{H/N}$  for fine particles revealed a typical seasonality, with the highest value  
413 occurring in winter (5.6) and the lowest value occurring in the spring (1.8). The  $R_{H/N}$   
414 for coarse particles was lower than that for fine particles, which ranged from 1.1 to  
415 1.9 and decreased as follows: summer > autumn > winter > spring. The higher  $R_{H/N}$   
416 values for fine particles further indicated the importance of fine particles in haze  
417 pollution.

418 We calculated the  $R_{H/N}$  ratios for chemical species in each size fraction. Based on  
419 the  $R_{H/N}$  ratios variations with increasing size fraction, all the species can be divided  
420 into three groups. First, OC,  $NO_3^-$ ,  $SO_4^{2-}$ ,  $NH_4^+$ ,  $K^+$ ,  $Cl^-$ , K, Mn, Ni, Cu, Zn, Pb and  
421 Tl exhibited high  $R_{H/N}$  ratios in fine mode and a peak value in size fraction 0.65-1.1

422  $\mu\text{m}$  or 1.1-2.1  $\mu\text{m}$ . Second,  $R_{\text{H/N}}$  ratios of  $\text{Na}^+$ ,  $\text{Mg}^{2+}$ ,  $\text{Ca}^{2+}$ , Mg and Fe increased with  
423 increasing size fraction. Third, EC, Na, Al, Ca, Co, Mo, Cd, Ba, Th and U,  $R_{\text{H/N}}$  ratios  
424 of these species first increased and then decreased with increasing size fraction and  
425 exhibited highest  $R_{\text{H/N}}$  ratios in size fraction 1.1-2.1  $\mu\text{m}$ , 2.1-3.3  $\mu\text{m}$  or 3.3-4.7  $\mu\text{m}$ .

426 The annual average  $R_{\text{H/N}}$  of the chemical components in  $\text{PM}_{2.1}$  ranged from 0.8 to  
427 5.5, with values greater than 2.6 for  $\text{NO}_3^-$ ,  $\text{SO}_4^{2-}$ ,  $\text{NH}_4^+$ , Pb, Tl and Cd. This finding  
428 was consistent with the findings of previous studies (Tian et al., 2014; Sun et al.,  
429 2013), indicating that coal and motor vehicle sources played important roles in haze  
430 pollution (Li et al., 2013). Regarding the seasonal variations, the particulate mass and  
431 most of the species exhibited the highest  $R_{\text{H/N}}$  in winter, which indirectly showed that  
432 severe haze events primarily occurred in winter.

433 Simultaneously, the annual average  $R_{\text{H/N}}$  of the chemical components in  $\text{PM}_{2.1-9}$   
434 ranged from 0.8 to 5.3, which was similar to that for fine particles. The  $\text{NH}_4^+$ ,  $\text{NO}_3^-$ ,  
435  $\text{SO}_4^{2-}$ , Cd, EC,  $\text{Cl}^-$ , Pb, Tl,  $\text{Na}^+$ , OC, Zn and  $\text{K}^+$  in the coarse fraction exhibited  $R_{\text{H/N}}$   
436 values greater than 1.4. Among these species, Pb, Cd and Tl had high toxicity. Thus,  
437 the mitigation of particles with diameters greater than 2.1  $\mu\text{m}$  cannot be neglected  
438 during haze events. Similar to  $\text{PM}_{2.1}$ , most of the species in the coarse fraction  
439 exhibited the highest  $R_{\text{H/N}}$  in winter. In contrast, the highest  $R_{\text{H/N}}$  values for  $\text{Na}^+$ ,  $\text{K}^+$   
440 and  $\text{Cl}^-$  in the coarse fraction were observed in summer, which was similar to the  
441 results of the mass concentration. The highest  $R_{\text{H/N}}$  for  $\text{Na}^+$ ,  $\text{K}^+$  and  $\text{Cl}^-$  in the coarse  
442 fraction was observed in summer, mainly due to low concentrations on non-haze days  
443 and relatively high concentration of haze days. The lower concentrations of coarse  
444 particles in summer were likely related to greater precipitation during this season.  
445 High concentrations of  $\text{K}^+$  and  $\text{Cl}^-$  in coarse mode on haze days were mainly  
446 associated with biomass burning (Du et al., 2011). One of the samples that  
447 represented a haze day in summer was collected between June 17 and 19. During this  
448 period, burning wheat straw in the surrounding areas affected both fine and coarse  
449 particle pollution in Beijing (Wang et al., 2015; Yan et al., 2015; Cheng et al., 2014).

450 The concentrations of  $\text{NO}_3^-$ ,  $\text{SO}_4^{2-}$  and  $\text{NH}_4^+$  in the fine and coarse particles were  
451 higher on haze days than on non-haze days. These species are involved in  
452 heterogeneous chemical reactions (Sun et al., 2013). Figs. S6a and b show good  
453 correlations between  $\text{NH}_4^+$  and  $\text{SO}_4^{2-}$  in fine particles from non-haze and haze days,  
454 with an equivalent  $\text{NH}_4^+/\text{SO}_4^{2-}$  ratio greater than unity (ranging from 1.5-1.6). This  
455 result reveals the dominance of  $(\text{NH}_4)_2\text{SO}_4$ . Next, we calculated the equivalent ratio of  
456  $\text{NH}_4^+$  to  $[\text{NO}_3^- + \text{SO}_4^{2-}]$  (Figs. S6c and d), which was slightly higher than unity on  
457 non-haze days and indicated the presence of  $\text{NH}_4\text{NO}_3$  in the fine mode aerosols.  
458 However, on haze days, the ratios were less than unity, which indicated that  $\text{NO}_3^-$   
459 may be present in chemical forms other than  $\text{NH}_4\text{NO}_3$ .

#### 460 4.1.2 Peak shifts

461 Fig. 3 compares the annual average mass concentration size distributions on  
462 non-haze and haze days, which were considered bimodal, with the peaks  
463 corresponding to the fine modes located at 0.65-1.1  $\mu\text{m}$  and those corresponding to  
464 the coarse modes peaking at 4.7-5.8  $\mu\text{m}$ . No significant differences in the average size  
465 distributions were found between haze and non-haze days in each season (Fig. 3).  
466 This result was inconsistent with the results obtained from early 2013, which showed  
467 that the peak mass concentration of fine mode particles shifted from 0.43-0.65  $\mu\text{m}$  on  
468 clear days to 0.65-1.1  $\mu\text{m}$  on lightly polluted days and 1.1-2.1  $\mu\text{m}$  on heavily polluted  
469 days (Tian et al., 2014). **During previous haze formation in Beijing, a continuous**  
470 **growth from the nucleation mode particles is also clearly depicted by the evolution in**  
471 **the mean particle size, which increases from about 40 nm when the  $\text{PM}_{2.5}$  level is less**  
472 **than  $50 \mu\text{g}\cdot\text{m}^{-3}$  to about 190 nm when the  $\text{PM}_{2.5}$  concentration exceeds  $300 \mu\text{g}\cdot\text{m}^{-3}$**   
473 **over the course of 3 d (Guo et al., 2014).**

474 However, in this study, peak shifts from 0.43-0.65  $\mu\text{m}$  on non-haze days to  
475 0.65-1.1  $\mu\text{m}$  on haze days were observed when considering the annual average size  
476 distributions of  $\text{SO}_4^{2-}$ ,  $\text{OC}$ ,  $\text{NO}_3^-$ ,  $\text{NH}_4^+$ ,  $\text{Cl}^-$ ,  $\text{K}^+$  and  $\text{Cd}$ . The peak values of these  
477 species at 0.43-0.65  $\mu\text{m}$  in the fine mode on non-haze days correspond to the

478 “condensation mode” due to the transformation of precursors and heterogeneous  
479 reactions, while those at 0.65-1.1  $\mu\text{m}$  on haze days correspond to the “droplet mode”,  
480 which likely form in clouds or through aqueous-phase chemical reactions (Sun et al.,  
481 2013). The high RH during haze days may facilitate the formation of “droplet mode”  
482 particles, and a similar finding was previously reported (Sun et al., 2013; Zhang et al.,  
483 2013a). However, this result was slightly different from that observed in early 2013,  
484 which showed that the peak concentration of  $\text{NH}_4^+$ ,  $\text{SO}_4^{2-}$  and  $\text{NO}_3^-$  in fine mode at  
485 1.1-2.1  $\mu\text{m}$  on heavily polluted days resulted from the high RH and high precursor  
486 concentrations (Tian et al., 2014).

487 We also compared size distributions of chemical species between haze and  
488 non-haze days in different seasons. The results showed that the peak concentration of  
489 OC,  $\text{SO}_4^{2-}$ ,  $\text{Cl}^-$  and Mn in fine mode particles shifted from 0.43-0.65  $\mu\text{m}$  on non-haze  
490 days to 0.65-1.1  $\mu\text{m}$  on haze days in spring. However, species exhibited peak shifts in  
491 summer were EC,  $\text{K}^+$ ,  $\text{NO}_3^-$  and Ni. Besides, in autumn, fine mode peak concentration  
492 of EC,  $\text{NH}_4^+$ ,  $\text{SO}_4^{2-}$ ,  $\text{NO}_3^-$ , Cd and Cu shifted from 0.43-0.65  $\mu\text{m}$  on non-haze days to  
493 0.65-1.1  $\mu\text{m}$  on haze days. Meanwhile,  $\text{NH}_4^+$ ,  $\text{SO}_4^{2-}$ ,  $\text{NO}_3^-$ ,  $\text{K}^+$ ,  $\text{Cl}^-$ , Cd, Zn and Pb  
494 exhibited fine mode peak shifts from non-haze days to haze days in winter. These  
495 indicated that there are different formation mechanisms for haze in different seasons.

#### 496 4.2 Mass closure studies

##### 497 4.2.1 Non-haze vs. haze days

498 Mass closure studies showed that SNA, OM and CM dominated the fine particles,  
499 which accounted for 87.7% and 76.6% of the  $\text{PM}_{2.5}$  mass on non-haze and haze days,  
500 respectively (Figs. 4a-d). Generally, the contribution of OM to  $\text{PM}_{2.5}$  was greater than  
501 the contributions of SNA and CM. However, during haze episodes in cold seasons,  
502 SNA was more significant than OM because the high RH and precursor emissions  
503 (i.e.,  $\text{SO}_2$ ) promoted the generation of SNA (Tian et al., 2014). **OM dominated in fine**  
504 **particles and decreased from 37.9% on non-haze days to 31.2% on haze days. Such an**  
505 **observation may reflect two distinct processes during haze formation in Beijing. New**

506 particle formation has been found to be prevalent in Beijing during clean period and  
507 the nucleation mode particles contained mainly secondary organics(Guo et al., 2014).  
508 Nucleation consistently precedes a polluted period, producing a high number  
509 concentration of nano-sized particles under clean conditions and the growth process  
510 competes with capture/removal of nano particles by coagulation with preexisting  
511 aerosols. In addition, there is also large evidence showing that organics play a key  
512 role in new particle formation, both to enhance aerosol nucleation and growth of  
513 freshly nucleated particles. For example, the interaction between organic and sulfuric  
514 acids promotes efficient formation of organic and sulfate aerosols in the polluted  
515 atmosphere (Zhang et al., 2004; Zhang et al., 2011). In contrast, the contribution of  
516 SNA to the PM<sub>2.1</sub> mass increased from 19.1% on non-haze days to 33.9% on haze  
517 days, indicating that SNA played a key role in haze formation. For haze pollution that  
518 is associated with high RH, the aqueous phase on the aerosol surface provides a  
519 means for the rapid heterogeneous gas-liquid conversion of gaseous precursors to  
520 produce secondary inorganic aerosols (Wang et al., 2012; Zhang et al., 2015b).

521 High total CM, OM and SNA contributions were also observed in PM<sub>2.1-9</sub>, which  
522 accounted for 58.5% and 54.3% of the total PM<sub>2.1-9</sub> mass on non-haze days and haze  
523 days, respectively. The contributions of these species in coarse particles decreased as  
524 follows on haze and non-haze days: CM > OM > SNA. However, in fine particles, the  
525 order was OM > CM > SNA on non-haze days and OM > SNA > CM on haze days.  
526 In summary, the relative contributions of OM and CM to the particle mass decreased  
527 from non-haze to haze days, and the relative contribution of SNA increased from  
528 non-haze days to haze days. Similar trends had been observed in previous Beijing  
529 haze study (Guo et al., 2014), in which the organic mass fraction dominates in the  
530 clean period (74–77%) and decreases slightly during the transition (48–49%) and  
531 polluted (35–42%) periods. The contributions of sulfate and nitrate to the particle  
532 mass concentration increase throughout the pollution period, with mass fractions of

533 8–9% and 6–12% for the clean period to 23–26% and 12–27% for the polluted period,  
534 respectively.

535 **4.2.2 Differences among size fractions**

536 For different size fractions, the contributions of OM, HM and EC were greatest in  
537 the < 0.43  $\mu\text{m}$  fraction (41.3%, 2.2% and 7.0%, respectively). The contribution of  
538 SNA, which is primarily formed from precursors via heterogeneous reactions, was  
539 greatest in the 0.43–0.65  $\mu\text{m}$  fraction (34.5%), which is within the “condensation  
540 mode” (Fig. 4e). The contribution decreased as the size increased, which indicated  
541 that these anthropogenic species primarily accumulated in the fine mode. However,  
542 the minimal contributions of OM, HM, EC and SNA occurred in the 5.8–9  $\mu\text{m}$   
543 (6.9%), > 9  $\mu\text{m}$  (0.7%), 4.7–5.8  $\mu\text{m}$  (0.9%) and > 9  $\mu\text{m}$  (4.1%) size fractions,  
544 respectively. In addition, CM and SS exhibited similar size fraction variations, which  
545 increased from < 0.43  $\mu\text{m}$  to 3.3–4.7  $\mu\text{m}$  and then decreased. The highest contributions  
546 of CM and SS appeared in the 3.3–4.7  $\mu\text{m}$  fraction and were 35.6% and 4.9%,  
547 respectively.

548 **4.2.3 Unidentified mass**

549 The reconstructed PM mass concentrations were compared with the gravimetric  
550 values, as shown in Fig. S7. The results were correlated with one another in the  
551 different size fractions, with  $R^2$  values for  $\text{PM}_{1.1}$  (particulate matter with aerodynamic  
552 diameter lower than 2.5  $\mu\text{m}$ ),  $\text{PM}_{2.1}$ ,  $\text{PM}_9$  and TSP (total suspended particulate matter)  
553 of 0.69, 0.79, 0.70 and 0.60, respectively. In addition, the contributions of the  
554 unidentified components ranged from 0.4% to 57.8% and increased as the sizes  
555 increased. The large unidentified components in the coarse particles potentially  
556 resulted from underestimating CM (Hueglin et al., 2005; Sun et al., 2004). In this  
557 study, Si was estimated as 3.42 times Al, and the ratios were applied to all of the size  
558 fractions. This assumption may be underestimated because the Si/Al ratio could  
559 increase with size. For example, the contribution of CM to coarse particles reached  
560 42.4% based on the Si/Al ratio of 6.0 in  $\text{PM}_{2.5-10}$ , which was previously reported in

561 Beijing (Zhang et al., 2010). Thus, the contribution of the unidentified components  
562 decreased from 38.5% to 25.5% for the total PM<sub>2.1-9</sub> mass.

### 563 **4.3 Source apportionment**

#### 564 **4.3.1 Fine and coarse particles**

565 Six PM<sub>2.1</sub> and seven PM<sub>2.1-9</sub> sources were identified by PMF analysis, respectively.  
566 Fig. 5(a) and (b) show the profiles of each source in the fine and coarse fractions,  
567 respectively, and the percentages of species apportioned by each source. The sources  
568 identified in the fine fraction were named as secondary inorganic aerosol (SIA), coal  
569 combustion, biomass burning, industrial pollution, road dust and vehicle emissions.  
570 Coarse fraction sources were SIA, coal combustion, biomass burning, industrial  
571 pollution, road dust, mineral dust and organic aerosol. Together these sources  
572 represented 91.6% and 86.6% of PM<sub>2.1</sub> and PM<sub>2.1-9</sub>, respectively.

#### 573 **Secondary inorganic aerosol**

574 The first source was relevant to SIA, which was identified in both fractions and  
575 was typically characterized by significant amounts of SO<sub>4</sub><sup>2-</sup>, NO<sub>3</sub><sup>-</sup> and NH<sub>4</sub><sup>+</sup>. SIA  
576 contributed 25.1% (16.9  $\mu\text{g m}^{-3}$ ) and 9.8% (6.1  $\mu\text{g m}^{-3}$ ) to the fine and coarse particles,  
577 respectively. Contributions of SIA to both PM<sub>2.1</sub> and PM<sub>2.1-9</sub> followed the order winter  
578 (29.5% to PM<sub>2.1</sub> and to 16.5 to PM<sub>2.1-9</sub>) > spring (27.2% and 9.3%) > autumn (20.3%  
579 and 7.8%) > summer (18.1% and 5.7%). The SIA contribution to the fine particles  
580 was similar to that in Beijing for 2009-2010 (Zhang et al., 2013b).

#### 581 **Coal combustion**

582 The second source, coal combustion, was also identified in both fractions and was  
583 characterized by elevated OC and EC, concentrations (Tian et al., 2010; Kang et al.,  
584 2011). The contribution of this source to PM<sub>2.1</sub> was 17.7% (11.9  $\mu\text{g m}^{-3}$ ), which  
585 closely approximates the value of 19% derived in Beijing for 2009-2010 (Zhang et al.,  
586 2013b). In addition to its contribution to PM<sub>2.1</sub>, coal combustion significantly  
587 contributed to PM<sub>2.1-9</sub> (7.8%, 4.9  $\mu\text{g m}^{-3}$ ). The contributions of coal combustion to  
588 PM<sub>2.1</sub> and PM<sub>2.1-9</sub> exhibited similar seasonal patterns of winter (27.0% to PM<sub>2.1</sub> and

589 9.4% to  $\text{PM}_{2.1-9}$ ) > autumn (17.5% and 8.9%) > summer (14.5% and 6.6%) > spring  
590 (9.6% and 6.4%).

### 591 **Biomass burning**

592 The third source, biomass burning, was also identified in both fractions and was  
593 represented by high  $\text{Cl}^-$  and  $\text{K}^+$  contents (also K, which is an excellent tracer of  
594 aerosols from biomass burning) (Du et al., 2011) and is rich in  $\text{Na}^+$  (Moon et al.,  
595 2008). The contribution in  $\text{PM}_{2.1}$  was 8.6%, which was significantly higher than the  
596 6.9% contribution in  $\text{PM}_{2.1-9}$ . This finding is expected because biomass burning  
597 contributed much more to the fine particles than the coarse particles (Cheng et al.,  
598 2014). Its contributions to  $\text{PM}_{2.1}$  and  $\text{PM}_{2.1-9}$  demonstrated a typical seasonal variation,  
599 with higher concentrations observed in spring (11.1% to  $\text{PM}_{2.1}$  and 11.8% to  $\text{PM}_{2.1-9}$ )  
600 and winter (13.5% and 10.2%).

### 601 **Industrial pollution**

602 The fourth source was industrial pollution, which was also identified in both  
603 fractions and was characterized by high Fe, Ni, Co, Mg, Al and Ca, contents in fine  
604 size fraction and by high Cd, Pb, Tl, Zn and Cu contents in coarse fraction (Karnae  
605 and John, 2011). The contribution from this source was 12.1%, which is slightly  
606 higher than the 5.1% contribution for coarse particles. Its contributions to  $\text{PM}_{2.1}$  and  
607  $\text{PM}_{2.1-9}$  demonstrated a typical seasonal variation, with higher concentrations observed  
608 in summer (16.7%) and autumn (14.5%) for fine fraction and with higher  
609 concentrations observed in winter (5.7%) and spring (7.9%).

### 610 **Road dust**

611 The fifth component, road dust, was also identified in both fractions and was  
612 related to the high loading of crustal elements, such as Al, Ca ( $\text{Ca}^{2+}$ ), Mg ( $\text{Mg}^{2+}$ ), Na  
613 ( $\text{Na}^+$ ) and Co, Ni, Cu (Titos et al., 2014; Vecchi et al., 2008). This source represented  
614 8.4% and 10.9% of the total mass in the fine and coarse fractions, respectively.  
615 Contributions of road dust to both  $\text{PM}_{2.1}$  and  $\text{PM}_{2.1-9}$  followed the order winter (9.9%  
616 to  $\text{PM}_{2.1}$  and to 18.3% to  $\text{PM}_{2.1-9}$ ) > autumn (10.2% and 16.0%) > spring (4.9% and

617 9.3%) > summer (6.3% and 4.7%).

618 **Vehicle emissions**

619 The sixth source, vehicle emissions, which was only identified in fine fraction and  
620 was characterized by high Pb, Cd, Zn, K and EC (Begum et al., 2004; Karnaee and  
621 John, 2011). EC primarily arises from engines; Zn and K are found in tailpipe  
622 emissions; Pb is present in motor and fuel oil combustion (Yang et al., 2013). This  
623 source explained 19.6% of PM<sub>2.5</sub>. Contributions of vehicle emissions PM<sub>2.5</sub> were  
624 higher in spring and summer. During 2000 and the period 2009-2010, the  
625 contributions from vehicles to the fine particles in Beijing were 7% and 4%,  
626 respectively (Zheng et al., 2005; Zhang et al., 2013b), and these values were lower  
627 than those reported in this study. The source in previous studies might be primary  
628 emissions from vehicles, however, in addition to primary emissions; vehicles also  
629 emit large amounts of NO<sub>x</sub> precursors, which contributed significantly to the PM via  
630 the generation of secondary particles. This important contribution was included in  
631 the SIA source but not in the primary emissions factor. Thus, the contributions of  
632 traffic emissions to PM will be much higher than the present value if we further  
633 consider the secondary formation of NO<sub>3</sub><sup>-</sup> from NO<sub>x</sub>. Besides, vehicles equipped  
634 with three-way catalysts are an important source of NH<sub>3</sub>, which may also contribute  
635 to the SIA.

636 **Mineral dust**

637 The seventh component, mineral dust, was only identified in coarse fraction and  
638 was related to the high loading of crustal elements, such as Al, Fe, Ca (Ca<sup>2+</sup>), Mg, K  
639 (K<sup>+</sup>) (Titos et al., 2014; Vecchi et al., 2008) This source might mainly indicate local  
640 and long-range transported dust aerosols and represented 22.6% to the total mass in  
641 coarse fraction. It exhibited a typical seasonal variation, with higher concentrations  
642 observed in spring (36.2%).

643 **Organic aerosol**

644 The eighth source was relevant to organic aerosol, which was only identified in

645 coarse fraction and was typically characterized by significant amounts of OC. Organic  
646 aerosol contributed 23.6% ( $14.7 \mu\text{g m}^{-3}$ ) to the coarse particles. Its contributions to  
647  $\text{PM}_{2.1-9}$  demonstrated a typical seasonal variation, with higher concentrations observed  
648 in summer (51.3%).

649 **4.3.2 Non-haze vs. haze days**

650 Figs. 6a-d illustrate the contributions of the six sources to the fine and seven  
651 source to the coarse particles on clear and haze days. On haze days, the contributions  
652 of SIA, coal combustion, biomass burning, industrial pollution, road dust and vehicle  
653 emissions, were 18.4%, 13.8%, 16.0%, 12.5%, 12.8% and 17.5% to the fine fractions  
654 and the contributions of SIA, coal combustion, biomass burning, industrial pollution,  
655 road dust, mineral dust and organic aerosol were 13.4%, 8.7%, 7.8%, 5.2%, 8.3%,  
656 24.4% and 19.5% to the coarse fractions. The contributions of these factors on haze  
657 days were higher than those on non-haze days, except road dust, and industrial  
658 pollution to fine fraction and mineral dust to coarse fraction particles. Additionally,  
659 the  $R_{H/N}$  of the six sources was highest for SIA (6.9 to fine particles vs. 10.1 to coarse  
660 particles), followed by vehicle emissions (4.3 to fine particles), biomass burning (2.8  
661 vs. 2.2), coal combustion (1.9 vs. 2.5), mineral dust (1.7 to coarse particles), organic  
662 aerosol (1.47 to coarse particles), industrial pollution (1.2 vs. 2.1) and, finally, road  
663 dust (0.7 vs. 0.7). The high  $R_{H/N}$  values indicated that enhanced secondary conversion  
664 could occur in the atmosphere during heavy-pollution days. Furthermore, primary  
665 particles and gaseous precursors from coal combustion and traffic emissions played  
666 important roles in haze pollution.

667 The strong contribution of mineral dust and road dust on non-haze days was  
668 primarily due to high wind speeds, which transported large quantities of particles from  
669 nearby areas outside of the city. Similarly, the industrial pollution affecting urban  
670 Beijing primarily arose from the surrounding areas, and the high wind speeds on  
671 non-haze days transported large quantities of industrial emission particles into Beijing  
672 from outside areas. However, on haze days, particles from coal combustion, primary

673 emissions from vehicles, biomass burning and secondary formation were important.  
674 Thus, strict control over particles and gaseous precursor emissions from coal and oil  
675 combustion is required.

676 **4.3.3 Difference among the size fractions**

677 Fig. 7 shows that the relative contributions of each identified source varied  
678 substantially among size fractions. Among all the sources, SIA and mineral dust (road  
679 dust for fine fractions and road dust plus mineral dust for coarse fractions), which  
680 were also identified in the mass closure analyses, exhibited relative orders in the eight  
681 size fractions that were similar to those in the mass closure results. However, the  
682 contributions of SIA in the eight size fractions were different from the contributions  
683 of SNA obtained by mass closure (i.e., 3.2-30.4% for SIA vs. 4.1-34.5% for SNA).  
684 The contribution of mineral dust increased with particle size, with the highest  
685 contribution found observed in the 3.3-4.7  $\mu\text{m}$  fraction (37.4%) and the lowest  
686 contribution observed in the 0.65-1.1  $\mu\text{m}$  fraction (5.2%). These results were  
687 consistent with the mass closure results, which indirectly verified the reliability of the  
688 PMF results.

689 The contributions of the other sources (coal combustion, biomass burning,  
690 industrial pollution) generally decreased with increasing size fraction and were  
691 present at high concentrations in the fine and coarse modes. For example, the  
692 contributions of coal combustion to the total mass in the different size fractions  
693 ranged from 7.2% to 42.2%, with the highest proportion found in the <0.43  $\mu\text{m}$   
694 fraction (42.2%) and a relatively high proportion found in the 3.3-4.7  $\mu\text{m}$  fraction  
695 (8.5%). Similarly, the contributions of industrial pollution ranged from 2.4% (5.8-9  
696  $\mu\text{m}$ ) to 15.9% (<0.43  $\mu\text{m}$ ). The concentrations of biomass burning were approximately  
697 8% with high proportions in the fine (< 0.43  $\mu\text{m}$ ) and (1.1-2.1  $\mu\text{m}$ ). The complexity of  
698 the source apportionment results for different size fractions indirectly verifies that the  
699 source apportionment of  $\text{PM}_{2.5}$  cannot provide comprehensive source information  
700 because it neglects the importance of the sources that dominated the coarse size

701 fractions. For example, the highest proportion of industrial pollution was observed in  
702 the 3.3-4.7  $\mu\text{m}$  size fraction.

703 To further examine the importance of source apportionment in the different size  
704 fractions, we compared the source apportionment results for the corresponding size  
705 sub-fractions within  $\text{PM}_{2.1}$  and  $\text{PM}_{2.1-9}$ . As shown in Fig. 7, the contributions of each  
706 source to PM significantly varied among the size fractions within  $\text{PM}_{2.1}$  and  $\text{PM}_{2.1-9}$ .  
707 The contributions of SIA, coal combustion, vehicle emissions and road dust to the size  
708 fractions within  $\text{PM}_{2.1}$  ranged from 8.9% to 30.4%, from 10.1% to 42.2%, from 11.4%  
709 to 27.7% and from 5.2% to 10.5%, respectively. In addition, significant differences  
710 were observed among the size fractions within  $\text{PM}_{2.1-9}$  regarding the contributions of  
711 SIA, industrial pollution and organic aerosol, which ranged from 3.2% to 23.6%, from  
712 2.4% to 8.5% and from 13.8% to 27.9%, respectively. This result further indicated the  
713 importance of source apportionment for subdivided size fractions within  $\text{PM}_{2.1}$  and  
714  $\text{PM}_{2.1-9}$ .

#### 715 **4.3.4 Back trajectory cluster analysis**

716 Approximately 34% of  $\text{PM}_{2.5}$  in urban Beijing can be attributed to sources outside  
717 of Beijing, and the contribution increased 50-70% during sustained wind flow from  
718 the south Hebei Province (Streets et al., 2007). This modeling result indicated the  
719 importance of the regional transport effect on fine particles in urban Beijing. However,  
720 the source apportionment based on size-resolved chemical measurements was  
721 previously unavailable.

722 To fill this gap, the annual data were subjected to back trajectory cluster analysis  
723 to identify the source regions and primary atmospheric circulation pathways that  
724 influence the PM concentration and chemical species (Fig. 8). The air masses that  
725 reach Beijing follow seven main paths, including four from the northwest (NW, C1,  
726 C2, C5 and C7) and one from southwest (SW, C3), one from the southeast (SE, C4)  
727 and one from the northeast (NE, C6). Fig. S8 shows the size distributions of the mass  
728 concentrations within each trajectory cluster. The size distributions of the mass

729 concentrations reveal large differences between the different trajectory clusters in the  
730 fine mode, especially in the peak size fraction (0.65-1.1  $\mu\text{m}$ ).

731 Because regional transport has stronger impacts on fine particles than on coarse  
732 particles, with the largest differences observed between trajectory clusters, we only  
733 report the identified  $\text{PM}_{2.5}$  sources associated with different trajectory clusters to  
734 determine the effects of the different source regions (Fig. 8). The polluted air mass  
735 trajectories are defined as those with  $\text{PM}_{2.5}$  concentrations higher than the annual  
736 mean of  $67.3 \mu\text{g m}^{-3}$ .

737 Although the greatest proportion of the trajectories (approximately 36%) was  
738 assigned to the NW cluster, this cluster was associated with the lowest  $\text{PM}_{2.5}$   
739 concentration of  $47.6 \mu\text{g m}^{-3}$ . Thus, this cluster has a weaker effect on PM pollution in  
740 Beijing. The long and rapidly moving trajectories were disaggregated into this group,  
741 and members of this cluster have extremely long transport patterns in which some  
742 parts cross over Mongolia, Inner Mongolia and northwest Hebei. In addition, this  
743 cluster was dominated by coal combustion (19%) and SIA (18%).

744 The SW cluster is the most important transport pathway with a large number of  
745 trajectories (approximately 32%) and a high  $\text{PM}_{2.5}$  concentration ( $79.9 \mu\text{g m}^{-3}$ ). The  
746 trajectories belonging to the SW cluster are characterized by the shortest trajectories,  
747 which indicate the closest and slowest-moving air masses that are primarily  
748 transported from Hebei and south Beijing. Most of the extreme episodes in this group  
749 were probably enriched by regional and local emission sources. As shown in Fig. 8,  
750 this cluster was dominated by SIA (27%) and coal combustion (19%).

751 As shown in Fig. 8, only 15% and 16% of the trajectories were assigned to the SE  
752 and NE clusters, respectively. However, these trajectories were associated with high  
753  $\text{PM}_{2.5}$  concentrations ( $87.0$  and  $67.4 \mu\text{g m}^{-3}$ ). The SE cluster typically followed a flow  
754 pattern over north Jiangsu and Shandong and was dominated by SIA (31%) and  
755 vehicle emissions (28%). In addition, the NE cluster, which crossed over the Liaoning  
756 Province and Tianjin, was dominated by SIA (25%), vehicle emissions (22%) and

757 coal combustion (20%). These results show that southern flows were dominant in  
758 urban Beijing and were associated with higher SIA, vehicle emissions and coal  
759 combustion contributions. Because SIA is primarily attributed to the transformation of  
760 precursors that originate from oil and coal combustion (i.e., NO<sub>x</sub> and SO<sub>2</sub>), controlling  
761 oil and coal combustion in the southern regions is required.

762 **4.4 Reconstructing the visibility**

763 In addition to particle size distributions, various chemical components play  
764 significant but different roles in reducing visibility on haze days. To further  
765 investigate the effects of the chemical species in the different size fractions and  
766 meteorological factors on visibility, correlation analyses were performed and  
767 regression model was used. SPSS 16.0 was used for multiple linear regression  
768 analysis (Cheng et al., 2011).

769 In this study, 93 variables were investigated; however, only 7 variables were  
770 selected because they had high correlation coefficients (> 0.5) with visibility. Overall,  
771 the results (Table S3) showed that visibility had high correlation coefficients (> 0.5)  
772 with SO<sub>4</sub><sup>2-</sup> in the 0.43-0.65  $\mu\text{m}$  and 0.65-1.1  $\mu\text{m}$  size fractions, NH<sub>4</sub><sup>+</sup> in the 0.43-0.65  
773  $\mu\text{m}$  and NO<sub>3</sub><sup>-</sup> in the 0.65-1.1  $\mu\text{m}$  size fractions and Ca<sup>2+</sup> in the 5.8-9  $\mu\text{m}$  size fraction  
774 as well as the RH and WS. All of the parameters that significantly affected visibility  
775 were used as inputs in the multiple linear regression models to simulate visibility.  
776 Ultimately, we developed the following regression equation for urban visibility in  
777 Beijing (Line 756-757).

778  $\text{Visibility} = 13.543 - 9.214\text{RH} + 2.069\text{WS} - 0.06[\text{NH}_4^+]_{0.43-0.65} - 0.037[\text{SO}_4^{2-}]_{0.43-0.65} - 0.44$   
779  $5[\text{SO}_4^{2-}]_{0.65-1.1} - 0.186[\text{NO}_3^-]_{0.65-1.1} - 2.18[\text{Ca}^{2+}]_{5.8-9}$

780 Previously, SO<sub>4</sub><sup>2-</sup>, NO<sub>3</sub><sup>-</sup> and NH<sub>4</sub><sup>+</sup> in PM<sub>2.5</sub> were reported to play important roles  
781 in visibility degradation during haze events in Beijing (Zhang et al., 2015a).  
782 Compared with previous studies, this study provides additional insights into the  
783 effects of chemical species in different size fractions on the visibility.

784 In addition, the RH, WS and  $\text{Ca}^{2+}$  content are important for explaining changes in  
785 visibility. High RH is conducive to the hygroscopic growth of particulate matter and  
786 the generation of secondary species and reduces the visibility. In addition,  $\text{Ca}^{2+}$   
787 crucially affects visibility because it associated with dust, which strongly reduces  
788 visibility. By contrast, high wind speeds are favorable for the diffusion of fine  
789 particles and can improve visibility.

790  $\text{NH}_4^+$  in the 0.43-0.65  $\mu\text{m}$  size fraction,  $\text{SO}_4^{2-}$  in the 0.65-1.1  $\mu\text{m}$  size fraction, and  
791  $\text{NO}_3^-$  in the 0.65-1.1  $\mu\text{m}$  size fraction are also among the most important factors that  
792 affect visibility. These species primarily accumulated in the submicron particles.  
793 Because the  $\text{SO}_4^{2-}$ ,  $\text{NO}_3^-$  and  $\text{NH}_4^+$  in this size fraction primarily originated from  
794 gaseous precursors ( $\text{NH}_3$ ,  $\text{NO}_2$  and  $\text{SO}_2$ ), regulations that control gaseous emissions of  
795 these precursors are important for reducing PM pollution and therefore improving  
796 visibility.

797 Our findings were similar to those reported for Jinan, in which the  $\text{SO}_4^{2-}$  and  
798 water content in the 1.0-1.8  $\mu\text{m}$  fraction and the RH were the most important factors  
799 that affected visibility (Cheng et al., 2011). However, in this study, the  $\text{Ca}^{2+}$  in the  
800 coarse particles, which primarily originated from construction dust and dust  
801 transported over long distances (Liu et al., 2014a; Maenhaut et al., 2002), also played  
802 an important role in reducing the visibility in urban Beijing. However, the transport of  
803 over long distances is not easy to control. Thus, we stress that construction dust must  
804 be controlled to improve visibility.

805 To validate the above equation, datasets from other periods (from March 2012 to  
806 February 2013) were used to characterize the relationships between visibility and  
807 chemical species (Miao, 2014). As shown in Fig. S9, the estimated visibility was well  
808 correlated with the measured visibility ( $R^2 = 0.87$ ,  $p < 0.05$ ). However, the ratio of the  
809 estimated visibility to the measured visibility was only 0.78, and discrete points  
810 primarily appeared for visibilities greater than 10 km (clear days). After scaling down,  
811 i.e., using datasets with visibilities less than 10 km to validate the above equation, the

812 ratio of the estimated visibility to the measured visibility reached 1.15 and  $R^2$  reached  
813 0.97. This result indicated that the species that resulted in reduced visibility were  
814 different for haze and clear conditions. This result is another indication that the above  
815 equation can characterize the relationship between visibility and chemical species  
816 during haze periods with a visibility of less than 10 km. This result will be useful for  
817 reconstructing the relationships between visibility and particulate matter source and  
818 we will do more discussion regarding this topic in the future.

819 **.5. Summary and conclusions**

820 The analysis of size-segregated airborne particles collected in Beijing from March  
821 1, 2013 to February 28, 2014 was presented. The annual average mass concentrations  
822 of the fine and coarse particles were higher than the National Ambient Air Quality  
823 Standard (Grade I) of China. The OC,  $SO_4^{2-}$ ,  $NO_3^-$  and  $NH_4^+$  species were the most  
824 abundant in the fine particles, accounting for 24.5%, 14.7%, 11.2% and 9.2% of the  
825  $PM_{2.1}$  mass, respectively. In  $PM_{2.1-9}$ , the primary chemical components were Ca  
826 (16.3%) and OC (15.5%). SOC, which formed due to photochemical reactions,  
827 primarily accumulated in the “condensation mode”. The size distribution of the OC  
828 peaked at 0.43-0.65  $\mu m$  in summer and at 0.65-1.1  $\mu m$  in winter.

829 The dataset excluding extreme weather events (i.e., rain, snow, fog and dust) was  
830 categorized into non-haze and haze days.  $NO_3^-$ ,  $SO_4^{2-}$ ,  $NH_4^+$ , Pb, Tl and Cd in  $PM_{2.1}$   
831 accumulated heavily during haze periods with  $R_{H/N} > 2.6$ . In coarse particles, the  $R_{H/N}$   
832 values of  $NH_4^+$ ,  $NO_3^-$ ,  $SO_4^{2-}$ , Cd, EC,  $Cl^-$ , Pb, Tl,  $Na^+$ , OC, Zn and  $K^+$  were also  
833 greater than unity, indicating that the effect of particles with a diameter larger than 2.1  
834  $\mu m$  cannot be neglected. The annual average size distributions of  $SO_4^{2-}$ , OC,  $NO_3^-$ ,  
835  $NH_4^+$ ,  $Cl^-$ ,  $K^+$  and Cd exhibited peak shifts from 0.43-0.65  $\mu m$  on non-haze days to  
836 0.65-1.1  $\mu m$  on haze days. In addition, a regression equation was developed to  
837 characterize the relationship between the visibility and the chemical species  
838 concentrations when the visibility was less than 10 km.

839 The mass closure results showed that OM, SNA and CM dominated the fine and

840 coarse particulate mass concentrations. Although OM **dominated** in fine particles, it  
841 decreased from 37.9% on non-haze days to 31.2% on haze days. In contrast, the  
842 contribution of SNA to the PM<sub>2.1</sub> mass increased from 19.1% on non-haze days to  
843 33.9% on haze days, indicating that SNA played a key role in haze formation.  
844 Moreover, the SNA, OM, HM and EC contributions decreased as the size increased,  
845 whereas those of CM and SS exhibited the opposite trend. Further studies are required  
846 to determine the identities of the unidentified components in the larger size fractions.

847 Six PM<sub>2.1</sub> sources and seven PM<sub>2.1-9</sub> sources were identified using the PMF  
848 method based on the annual size-segregated data. The source concentrations varied  
849 between non-haze and haze days. The results show that coal combustion, vehicle  
850 emissions, industrial pollution, biomass burning and secondary formation were major  
851 contributors on haze days. In contrast, mineral dust (road dust) was important source  
852 on non-haze days. In addition, the relative contributions of these sources in Beijing  
853 varied significantly as the fraction sizes changed. The contributions of all of the  
854 sources decreased as the size of the fraction increased with the exception of mineral  
855 dust; however, they exhibited relatively high proportions in the fine and coarse modes,  
856 indicating the importance of source apportionment for size sub-fractions within PM<sub>2.1</sub>  
857 and PM<sub>2.1-9</sub>. Combining these findings with the trajectory clustering results, the source  
858 regions associated with PM<sub>2.1</sub> in Beijing were further explored. We found that the  
859 southern and northeastern flows are associated with greater SIA, vehicle emissions  
860 and coal combustion contributions, whereas the northwestern flows transport more  
861 mineral dust.

## 862 **Acknowledgements**

863 This study supported by the “Strategic Priority Research Program” of the Chinese  
864 Academy of Sciences (XDB05020000 and XDA05100100), the National Natural  
865 Science Foundation of China (No.: 41405144, 41230642 and 41321064). And  
866 Haze Observation Project Especially for Jing-Jin-Ji Area (HOPE-J<sup>3</sup>A)(No.:KJZD-EW  
867 -TZ-G06-01-04).

868 **References**

869 Begum, B. A., Kim, E., Biswas, S. K., and Hopke, P. K.: Investigation of sources of  
870 atmospheric aerosol at urban and semi-urban areas in Bangladesh, *Atmos Environ*, 38,  
871 3025-3038, 10.1016/j.atmosenv.2004.02.042, 2004.

872 Bullock, K. R., Duvall, R. M., Norris, G. A., McDow, S. R., and Hays, M. D.:  
873 Evaluation of the CMB and PMF models using organic molecular markers in fine  
874 particulate matter collected during the Pittsburgh Air Quality Study, *Atmos Environ*,  
875 42, 6897-6904, 10.1016/j.atmosenv.2008.05.011, 2008.

876 Cao, J., Lee, S., Chow, J. C., Watson, J. G., Ho, K., Zhang, R., Jin, Z., Shen, Z., Chen,  
877 G., and Kang, Y.: Spatial and seasonal distributions of carbonaceous aerosols over  
878 China, *J Geophys Res D*, 112, doi:10.1029/2006JD008205,  
879 doi:10.1029/2006JD008205, 2007.

880 Chan, C. Y., Xu, X. D., Li, Y. S., Wong, K. H., Ding, G. A., Chan, L. Y., and Cheng,  
881 X. H.: Characteristics of vertical profiles and sources of PM<sub>2.5</sub>, PM<sub>10</sub> and  
882 carbonaceous species in Beijing, *Atmos Environ*, 39, 5113-5124,  
883 10.1016/j.atmosenv.2005.05.009, 2005.

884 Cheng, S.-h., Yang, L.-x., Zhou, X.-h., Xue, L.-k., Gao, X.-m., Zhou, Y., and Wang,  
885 W.-x.: Size-fractionated water-soluble ions, situ pH and water content in aerosol on  
886 hazy days and the influences on visibility impairment in Jinan, China, *Atmos Environ*,  
887 45, 4631-4640, 10.1016/j.atmosenv.2011.05.057, 2011.

888 Cheng, Y., Engling, G., He, K. b., Duan, F. k., Du, Z. y., Ma, Y. l., Liang, L. l., Lu, Z.  
889 f., Liu, J. m., Zheng, M., and Weber, R. J.: The characteristics of Beijing aerosol  
890 during two distinct episodes: Impacts of biomass burning and fireworks, *Environ  
891 Pollut*, 185, 149-157, 10.1016/j.envpol.2013.10.037, 2014.

892 Contini, D., Cesari, D., Genga, A., Siciliano, M., Ielpo, P., Guascito, M. R., and Conte,  
893 M.: Source apportionment of size-segregated atmospheric particles based on the major  
894 water-soluble components in Lecce (Italy), *Sci Total Environ*, 472, 248-261,  
895 10.1016/j.scitotenv.2013.10.127, 2014.

896 Du, H., Kong, L., Cheng, T., Chen, J., Du, J., Li, L., Xia, X., Leng, C., and Huang, G.:  
897 Insights into summertime haze pollution events over Shanghai based on online  
898 water-soluble ionic composition of aerosols, *Atmos Environ*, 45, 5131-5137,  
899 10.1016/j.atmosenv.2011.06.027, 2011.

900 Du, Z., He, K., Cheng, Y., Duan, F., Ma, Y., Liu, J., Zhang, X., Zheng, M., and  
901 Weber, R.: A year long study of water-soluble organic carbon in Beijing II: Light  
902 absorption properties, *Atmos Environ*, 89, 235-241, 10.1016/j.atmosenv.2014.02.022,  
903 2014.

904 Duan, F., He, K., Ma, Y., Jia, Y., Yang, F., Lei, Y., Tanaka, S., and Okuta, T.:  
905 Characteristics of carbonaceous aerosols in Beijing, China, *Chemosphere*, 60,  
906 355-364, 10.1016/j.chemosphere.2004.12.035, 2005.

907 Duarte, R. M. B. O., Mieiro, C. L., Penetra, A., Pio, C. A., and Duarte, A. C.:  
908 Carbonaceous materials in size-segregated atmospheric aerosols from urban and

909 coastal-rural areas at the Western European Coast, *Atmos Res*, 90, 253-263,  
910 10.1016/j.atmosres.2008.03.003, 2008.

911 Fisher, J. A., Jacob, D. J., Wang, Q., Bahreini, R., Carouge, C. C., Cubison, M. J.,  
912 Dibb, J. E., Diehl, T., Jimenez, J. L., Leibensperger, E. M., Lu, Z., Meinders, M. B. J.,  
913 Pye, H. O. T., Quinn, P. K., Sharma, S., Streets, D. G., van Donkelaar, A., and  
914 Yantosca, R. M.: Sources, distribution, and acidity of sulfate–ammonium aerosol in  
915 the Arctic in winter–spring, *Atmos Environ*, 45, 7301-7318,  
916 10.1016/j.atmosenv.2011.08.030, 2011.

917 Gao, J., Chai, F., Wang, T., Wang, S., and Wang, W.: Particle number size  
918 distribution and new particle formation: New characteristics during the special  
919 pollution control period in Beijing, *J Environ Sci*, 24, 14-21,  
920 10.1016/S1001-0742(11)60725-0, 2012.

921 Guo, S., Hu, M., Wang, Z. B., Slanina, J., and Zhao, Y. L.: Size-resolved aerosol  
922 water-soluble ionic compositions in the summer of Beijing: implication of regional  
923 secondary formation, *Atmos Chem Phys*, 10, 947-959, 10.5194/acp-10-947-2010,  
924 2010.

925 Guo, S., Hu, M., Zamora, M. L., Peng, J., Shang, D., Zheng, J., Du, Z., Wu, Z., Shao,  
926 M., Zeng, L., Molina, M. J., and Zhang, R.: Elucidating severe urban haze formation  
927 in China, *Proceedings of the National Academy of Sciences of the United States of  
928 America*, 111, 17373-17378, 10.1073/pnas.1419604111, 2014.

929 Hou, B., Zhuang, G., Zhang, R., Liu, T., Guo, Z., and Chen, Y.: The implication of  
930 carbonaceous aerosol to the formation of haze: Revealed from the characteristics and  
931 sources of OC/EC over a mega-city in China, *J Hazard Mater*, 190, 529-536,  
932 10.1016/j.jhazmat.2011.03.072, 2011.

933 Huang, R. J., Zhang, Y. L., Bozzetti, C., Ho, K. F., Cao, J. J., Han, Y. M.,  
934 Daellenbach, K. R., Slowik, J. G., Platt, S. M., Canonaco, F., Zotter, P., Wolf, R.,  
935 Pieber, S. M., Bruns, E. A., Crippa, M., Ciarelli, G., Piazzalunga, A., Schwikowski,  
936 M., Abbaszade, G., Schnelle-Kreis, J., Zimmermann, R., An, Z. S., Szidat, S.,  
937 Baltensperger, U., El Haddad, I., and Prevot, A. S. H.: High secondary aerosol  
938 contribution to particulate pollution during haze events in China, *Nature*, 514,  
939 218-222, 10.1038/nature13774, 2014.

940 Hueglin, C., Gehrig, R., Baltensperger, U., Gysel, M., Monn, C., and Vonmont, H.:  
941 Chemical characterisation of PM<sub>2.5</sub>, PM<sub>10</sub> and coarse particles at urban, near-city and  
942 rural sites in Switzerland, *Atmos Environ*, 39, 637-651,  
943 10.1016/j.atmosenv.2004.10.027, 2005.

944 Jacobson, M. C., Hansson, H. C., Noone, K. J., and Charlson, R. J.: Organic  
945 atmospheric aerosols: Review and state of the science, *Rev Geophys*, 38, 267-294,  
946 10.1029/1998rg000045, 2000.

947 Jing, H., Li, Y.-F., Zhao, J., Li, B., Sun, J., Chen, R., Gao, Y., and Chen, C.:  
948 Wide-range particle characterization and elemental concentration in Beijing aerosol  
949 during the 2013 Spring Festival, *Environ Pollut*, 192, 204-211,  
950 10.1016/j.envpol.2014.06.003, 2014.

951 Kang, J., Choi, M.-S., Yi, H.-I., Song, Y.-H., Lee, D., and Cho, J.-H.: A five-year  
952 observation of atmospheric metals on Ulleung Island in the East/Japan Sea: Temporal  
953 variability and source identification, *Atmos Environ*, 45, 4252-4262,  
954 10.1016/j.atmosenv.2011.04.083, 2011.

955 Karanasiou, A. A., Siskos, P. A., and Eleftheriadis, K.: Assessment of source  
956 apportionment by Positive Matrix Factorization analysis on fine and coarse urban  
957 aerosol size fractions, *Atmos Environ*, 43, 3385-3395,  
958 10.1016/j.atmosenv.2009.03.051, 2009.

959 Karnaee, S., and John, K.: Source apportionment of fine particulate matter measured in  
960 an industrialized coastal urban area of South Texas, *Atmos Environ*, 45, 3769-3776,  
961 10.1016/j.atmosenv.2011.04.040, 2011.

962 Li, X., Wang, L., Wang, Y., Wen, T., Yang, Y., Zhao, Y., and Wang, Y.: Chemical  
963 composition and size distribution of airborne particulate matters in Beijing during the  
964 2008 Olympics, *Atmos Environ*, 50, 278-286, 10.1016/j.atmosenv.2011.12.021, 2012.

965 Li, X., Wang, L., Ji, D., Wen, T., Pan, Y., Sun, Y., and Wang, Y.: Characterization of  
966 the size-segregated water-soluble inorganic ions in the Jing-Jin-Ji urban  
967 agglomeration: Spatial/temporal variability, size distribution and sources, *Atmos  
968 Environ*, 77, 250-259, 10.1016/j.atmosenv.2013.03.042, 2013.

969 Liu, Q., Liu, Y., Yin, J., Zhang, M., and Zhang, T.: Chemical characteristics and  
970 source apportionment of PM10 during Asian dust storm and non-dust storm days in  
971 Beijing, *Atmos Environ*, 91, 85-94, 10.1016/j.atmosenv.2014.03.057, 2014a.

972 Liu, S., Hu, M., Slanina, S., He, L. Y., Niu, Y. W., Bruegemann, E., Gnauk, T., and  
973 Herrmann, H.: Size distribution and source analysis of ionic compositions of aerosols  
974 in polluted periods at Xinken in Pearl River Delta (PRD) of China, *Atmos Environ*, 42,  
975 6284-6295, 10.1016/j.atmosenv.2007.12.035, 2008.

976 Liu, Z. R., Hu, B., Liu, Q., Sun, Y., and Wang, Y. S.: Source apportionment of urban  
977 fine particle number concentration during summertime in Beijing, *Atmos Environ*,  
978 10.1016/j.atmosenv.2014.06.055, 2014b.

979 Maenhaut, W., Cafmeyer, J., Dubtsov, S., and Chi, X.: Detailed mass size  
980 distributions of elements and species, and aerosol chemical mass closure during fall  
981 1999 at Gent, Belgium, *Nuclear Instruments and Methods in Physics Research  
982 Section B: Beam Interactions with Materials and Atoms*, 189, 238-242,  
983 10.1016/s0168-583x(01)01049-7, 2002.

984 McFiggans, G.: ATMOSPHERIC SCIENCE Involatile particles from rapid oxidation,  
985 *Nature*, 506, 442-443, 10.1038/506442a, 2014.

986 Miao, H.: Spatial and temporal characterizations of water soluble inorganic ions of  
987 aerosol in China, *Institute of Atmosphere Physics, Chinese Academy of Science,  
988 Beijing*, 2014.

989 Moon, K. J., Han, J. S., Ghim, Y. S., and Kim, Y. J.: Source apportionment of fine  
990 carbonaceous particles by positive matrix factorization at Gosan background site in  
991 East Asia, *Environ Int*, 34, 654-664, 10.1016/j.envint.2007.12.021, 2008.

992 Paatero, P., and Tapper, U.: Positive matrix factorization: A non-negative factor  
993 model with optimal utilization of error estimates of data values, *Environmetrics*, 5,  
994 111-126, 10.1002/env.3170050203, 1994.

995 Paatero, P.: Least square formulation of robust non-negative factor analysis,  
996 *Chemometr Intell Lab*, 3, 23-35, 10.1016/S0169-7439(96)00044-5, 1997.

997 Pan, Y. P., Wang, Y. S., Tang, G. Q., and Wu, D.: Spatial distribution and temporal  
998 variations of atmospheric sulfur deposition in Northern China: insights into the  
999 potential acidification risks, *Atmos Chem Phys*, 13, 1675-1688,  
1000 10.5194/acp-13-1675-2013, 2013.

1001 Pan, Y. P., and Wang, Y. S.: Atmospheric wet and dry deposition of trace elements at  
1002 10 sites in Northern China, *Atmos Chem Phys*, 15, 951-972,  
1003 10.5194/acp-15-951-2015, 2015.

1004 Pant, P., and Harrison, R. M.: Critical review of receptor modelling for particulate  
1005 matter: A case study of India, *Atmos Environ*, 49, 1-12,  
1006 10.1016/j.atmosenv.2011.11.060, 2012.

1007 Pillai, P. S., and Moorthy, K. K.: Aerosol mass-size distributions at a tropical coastal  
1008 environment: response to mesoscale and synoptic processes, *Atmos Environ*, 35,  
1009 4099-4112, 10.1016/s1352-2310(01)00211-4, 2001.

1010 Quan, J., Tie, X., Zhang, Q., Liu, Q., Li, X., Gao, Y., and Zhao, D.: Characteristics of  
1011 heavy aerosol pollution during the 2012-2013 winter in Beijing, China, *Atmos  
1012 Environ*, 88, 83-89, 10.1016/j.atmosenv.2014.01.058, 2014.

1013 Schleicher, N., Norra, S., Fricker, M., Kaminski, U., Chen, Y., Chai, F., Wang, S., Yu,  
1014 Y., and Cen, K.: Spatio-temporal variations of black carbon concentrations in the  
1015 Megacity Beijing, *Environ Pollut*, 182, 392-401, 10.1016/j.envpol.2013.07.042, 2013.

1016 Sirois, A., and Bottenheim, J. W.: Use of backward trajectories to interpret the 5-year  
1017 record of PAN and O<sub>3</sub> ambient air concentrations at Kejimkujik National Park, Nova  
1018 Scotia, *J Geophys Res D*, 100, 2867-2881, 10.1029/94jd02951, 1995.

1019 Song, Y., Zhang, Y., Xie, S., Zeng, L., Zheng, M., Salmon, L. G., Shao, M., and  
1020 Slanina, S.: Source apportionment of PM2.5 in Beijing by positive matrix  
1021 factorization, *Atmos Environ*, 40, 1526-1537, 10.1016/j.atmosenv.2005.10.039, 2006.

1022 Song, Y., Tang, X., Xie, S., Zhang, Y., Wei, Y., Zhang, M., Zeng, L., and Lu, S.:  
1023 Source apportionment of PM2.5 in Beijing in 2004, *J Hazard Mater*, 146, 124-130,  
1024 10.1016/j.jhazmat.2006.11.058, 2007.

1025 Streets, D. G., Fu, J. S., Jang, C. J., Hao, J., He, K., Tang, X., Zhang, Y., Wang, Z., Li,  
1026 Z., Zhang, Q., Wang, L., Wang, B., and Yu, C.: Air quality during the 2008 Beijing  
1027 Olympic Games, *Atmos Environ*, 41, 480-492, 10.1016/j.atmosenv.2006.08.046,  
1028 2007.

1029 Sun, J., Zhang, Q., Canagaratna, M. R., Zhang, Y., Ng, N. L., Sun, Y., Jayne, J. T.,  
1030 Zhang, X., Zhang, X., and Worsnop, D. R.: Highly time- and size-resolved  
1031 characterization of submicron aerosol particles in Beijing using an Aerodyne Aerosol  
1032 Mass Spectrometer, *Atmos Environ*, 44, 131-140, 10.1016/j.atmosenv.2009.03.020,  
1033 2010.

1034 Sun, Y., Zhuang, G., Wang, Y., Han, L., Guo, J., Dan, M., Zhang, W., Wang, Z., and  
1035 Hao, Z.: The air-borne particulate pollution in Beijing—concentration, composition,  
1036 distribution and sources, *Atmos Environ*, 38, 5991-6004,  
1037 10.1016/j.atmosenv.2004.07.009, 2004.

1038 Sun, Y., Zhuang, G., Tang, A., Wang, Y., and An, Z.: Chemical characteristics of  
1039  $PM_{2.5}$  and  $PM_{10}$  in haze-fog episodes in Beijing, *Environ Sci Technol*, 40, 3148-3155,  
1040 2006.

1041 Sun, Z., Mu, Y., Liu, Y., and Shao, L.: A comparison study on airborne particles  
1042 during haze days and non-haze days in Beijing, *Sci Total Environ*, 456-457, 1-8,  
1043 10.1016/j.scitotenv.2013.03.006, 2013.

1044 Tan, J. H., Duan, J. C., Chen, D. H., Wang, X. H., Guo, S. J., Bi, X. H., Sheng, G. Y.,  
1045 He, K. B., and Fu, J. M.: Chemical characteristics of haze during summer and winter  
1046 in Guangzhou, *Atmos Res*, 94, 238-245, 10.1016/j.atmosres.2009.05.016, 2009.

1047 Tian, H. Z., Wang, Y., Xue, Z. G., Cheng, K., Qu, Y. P., Chai, F. H., and Hao, J. M.:  
1048 Trend and characteristics of atmospheric emissions of Hg, As, and Se from coal  
1049 combustion in China, 1980–2007, *Atmos Chem Phys*, 10, 11905-11919,  
1050 10.5194/acp-10-11905-2010, 2010.

1051 Tian, S., Pan, Y., Liu, Z., Wen, T., and Wang, Y.: Size-resolved aerosol chemical  
1052 analysis of extreme haze pollution events during early 2013 in urban Beijing, China, *J  
1053 Hazard Mater*, 279, 452-460, 10.1016/j.jhazmat.2014.07.023, 2014.

1054 Titos, G., Lyamani, H., Pandolfi, M., Alastuey, A., and Alados-Arboledas, L.:  
1055 Identification of fine ( $PM_1$ ) and coarse ( $PM_{10-1}$ ) sources of particulate matter in an  
1056 urban environment, *Atmos Environ*, 89, 593-602, 10.1016/j.atmosenv.2014.03.001,  
1057 2014.

1058 Vecchi, R., Chiari, M., D'Alessandro, A., Fermo, P., Lucarelli, F., Mazzei, F., Nava,  
1059 S., Piazzalunga, A., Prati, P., Silvani, F., and Valli, G.: A mass closure and PMF  
1060 source apportionment study on the sub-micron sized aerosol fraction at urban sites in  
1061 Italy, *Atmos Environ*, 42, 2240-2253, 10.1016/j.atmosenv.2007.11.039, 2008.

1062 Wang, G., Kawamura, K., Lee, S., Ho, K., and Cao, J.: Molecular, Seasonal, and  
1063 Spatial Distributions of Organic Aerosols from Fourteen Chinese Cities, *Environ Sci  
1064 Technol*, 40, 4619-4625, 10.1021/es060291x, 2006a.

1065 Wang, L., Xin, J., Li, X., and Wang, Y.: The variability of biomass burning and its  
1066 influence on regional aerosol properties during the wheat harvest season in North  
1067 China, *Atmos Res*, 157, 153-163, 10.1016/j.atmosres.2015.01.009, 2015.

1068 Wang, L. T., Wei, Z., Yang, J., Zhang, Y., Zhang, F. F., Su, J., Meng, C. C., and  
1069 Zhang, Q.: The 2013 severe haze over southern Hebei, China: model evaluation,  
1070 source apportionment, and policy implications, *Atmos Chem Phys*, 14, 3151-3173,  
1071 10.5194/acp-14-3151-2014, 2014.

1072 Wang, X., Wang, W., Yang, L., Gao, X., Nie, W., Yu, Y., Xu, P., Zhou, Y., and Wang,  
1073 Z.: The secondary formation of inorganic aerosols in the droplet mode through  
1074 heterogeneous aqueous reactions under haze conditions, *Atmos Environ*, 63, 68-76,  
1075 10.1016/j.atmosenv.2012.09.029, 2012.

1076 Wang, Y. Q., Zhang, X. Y., and Arimoto, R.: The contribution from distant dust  
1077 sources to the atmospheric particulate matter loadings at XiAn, China during spring,  
1078 *Sci Total Environ*, 368, 875-883, 10.1016/j.scitotenv.2006.03.040, 2006b.

1079 Yan, C., Zheng, M., Sullivan, A. P., Bosch, C., Desyaterik, Y., Andersson, A., Li, X.,  
1080 Guo, X., Zhou, T., Gustafsson, Ö., and Collett Jr, J. L.: Chemical characteristics and  
1081 light-absorbing property of water-soluble organic carbon in Beijing: Biomass burning  
1082 contributions, *Atmos Environ*, 10.1016/j.atmosenv.2015.05.005, 2015.

1083 Yang, L., Cheng, S., Wang, X., Nie, W., Xu, P., Gao, X., Yuan, C., and Wang, W.:  
1084 Source identification and health impact of PM<sub>2.5</sub> in a heavily polluted urban  
1085 atmosphere in China, *Atmos Environ*, 75, 265-269, 10.1016/j.atmosenv.2013.04.058,  
1086 2013.

1087 Yang, X., Chen, Y. Z., Liu, H. F., Zhao, Y. X., Gao, J., Chai, F. H., and Meng, F.:  
1088 Characteristics and formation mechanism of a serious haze event in January 2013 in  
1089 Beijing, *China Environ Sci*, 34, 282-288, 2014.

1090 Yang, Y., Wang, Y., Wen, T., Wei, L., Ya'nan, Z., and Liang, L.: Elemental  
1091 composition of PM2.5 and PM10 at Mount Gongga in China during 2006, *Atmos Res*,  
1092 93, 801-810, 10.1016/j.atmosres.2009.03.014, 2009.

1093 Yao, X., Lau, A. P. S., Fang, M., Chan, C. K., and Hu, M.: Size distributions and  
1094 formation of ionic species in atmospheric particulate pollutants in Beijing, China:  
1095 inorganic ions, *Atmos Environ*, 37, 2991-3000, 10.1016/S1352-2310(03)00255-3,  
1096 2003.

1097 Zhang, G., Bi, X., Chan, L. Y., Wang, X., Sheng, G., and Fu, J.: Size-segregated  
1098 chemical characteristics of aerosol during haze in an urban area of the Pearl River  
1099 Delta region, *China Urban Clim*, 4, 74-84, 10.1016/j.uclim.2013.05.002, 2013a.

1100 Zhang, H., Hu, J., Kleeman, M., and Ying, Q.: Source apportionment of sulfate and  
1101 nitrate particulate matter in the Eastern United States and effectiveness of emission  
1102 control programs, *Sci Total Environ*, 490, 171-181, 10.1016/j.scitotenv.2014.04.064,  
1103 2014a.

1104 Zhang, J. K., Sun, Y., Liu, Z. R., Ji, D. S., Hu, B., Liu, Q., and Wang, Y. S.:  
1105 Characterization of submicron aerosols during a month of serious pollution in Beijing,  
1106 2013, *Atmos Chem Phys*, 14, 2887-2903, 10.5194/acp-14-2887-2014, 2014b.

1107 Zhang, Q., Quan, J., Tie, X., Li, X., Liu, Q., Gao, Y., and Zhao, D.: Effects of  
1108 meteorology and secondary particle formation on visibility during heavy haze events  
1109 in Beijing, China, *Sci Total Environ*, 502, 578-584, 10.1016/j.scitotenv.2014.09.079,  
1110 2015a.

1111 Zhang, R., Suh, I., Zhao, J., Zhang, D., Fortner, E. C., Tie, X., Molina, L. T., and  
1112 Molina, M. J.: Atmospheric new particle formation enhanced by organic acids,  
1113 *Science*, 304, 1487-1490, 2004.

1114 Zhang, R., Khalizov, A., Wang, L., Hu, M., and Xu, W.: Nucleation and growth of  
1115 nanoparticles in the atmosphere, *Chem Rev*, 112, 1957-2011, 2011.

1116 Zhang, R., Jing, J., Tao, J., Hsu, S. C., Wang, G., Cao, J., Lee, C. S. L., Zhu, L., Chen,  
1117 Z., Zhao, Y., and Shen, Z.: Chemical characterization and source apportionment of

1118 PM<sub>2.5</sub> in Beijing: seasonal perspective, Atmos Chem Phys, 13, 7053-7074,  
1119 10.5194/acp-13-7053-2013, 2013b.  
1120 Zhang, R., Wang, G., Guo, S., Zamora, M. L., Ying, Q., Lin, Y., Wang, W., Hu, M.,  
1121 and Wang, Y.: Formation of Urban Fine Particulate Matter, Chem Rev, 2015b.  
1122 Zhang, W., Zhuang, G., Guo, J., Xu, D., Wang, W., Baumgardner, D., Wu, Z., and  
1123 Yang, W.: Sources of aerosol as determined from elemental composition and size  
1124 distributions in Beijing, Atmos Res, 95, 197-209, 10.1016/j.atmosres.2009.09.017,  
1125 2010.  
1126 Zhang, X. Y., Wang, Y. Q., Zhang, X. C., Guo, W., and Gong, S. L.: Carbonaceous  
1127 aerosol composition over various regions of China during 2006, J Geophys Res D,  
1128 113, D14111, 10.1029/2007jd009525, 2008.  
1129 Zheng, M., Salmon, L. G., Schauer, J. J., Zeng, L., Kiang, C., Zhang, Y., and Cass, G.  
1130 R.: Seasonal trends in PM<sub>2.5</sub> source contributions in Beijing, China, Atmos Environ,  
1131 39, 3967-3976, 2005.  
1132 Zhuang, X., Wang, Y., He, H., Liu, J., Wang, X., Zhu, T., Ge, M., Zhou, J., Tang, G.,  
1133 and Ma, J.: Haze insights and mitigation in China: An overview, J Environ Sci, 26,  
1134 2-12, 10.1016/S1001-0742(13)60376-9, 2014.  
1135

### 1136 **Figure captions**

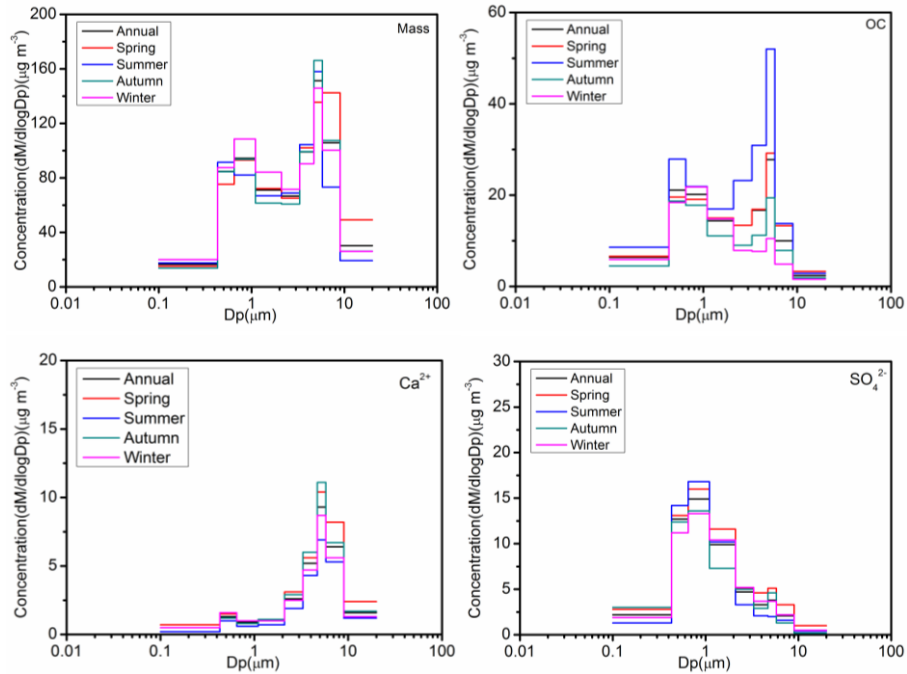
1137 Fig. 1 Mass concentration size distributions and that of typical chemical species in  
1138 different categories.  
1139 Fig. 2 Size-resolved mass concentration (distributions that are marked as solid circle  
1140 and open triangle denote haze and non-haze days, respectively).  
1141 Fig. 3 Mass concentration size distributions on haze and non-haze days over the entire  
1142 sampling period (annual) and by season as well as that of the typical chemical species.  
1143 Fig. 4 Contributions of different components to the total masses in (a) PM<sub>2.1</sub> on  
1144 non-haze days; (b) PM<sub>2.1</sub> on haze days; (c) PM<sub>2.1-9</sub> on non-haze days; (d) PM<sub>2.1-9</sub> on  
1145 haze days; (e) different size fractions.  
1146 Fig. 5 The profiles of each source in (a) fine and (b) coarse fractions.  
1147 Fig. 6 Relative contributions from each identified source to (a) PM<sub>2.1</sub> on non-haze  
1148 days; (b) PM<sub>2.1</sub> on haze days; (c) PM<sub>2.1-9</sub> on non-haze days; (d) PM<sub>2.1-9</sub> on haze days  
1149 and (e) mass concentrations of each source.  
1150 Fig. 7 Relative contributions from each identified source to different size fractions.

1151 Fig. 8 Relative contributions from each identified source to PM<sub>2.1</sub> at different  
1152 trajectory clusters.

1153

1154

1155



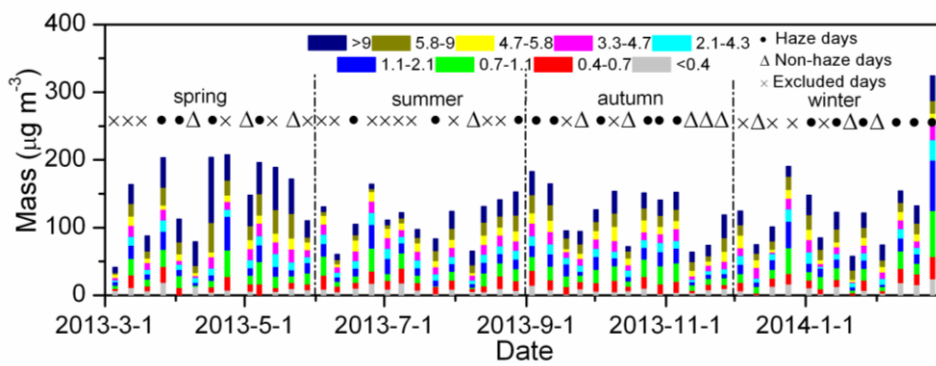
1156 Fig. 1 Mass concentration size distributions and that of typical chemical species in  
1157 different categories.  
1158

1159

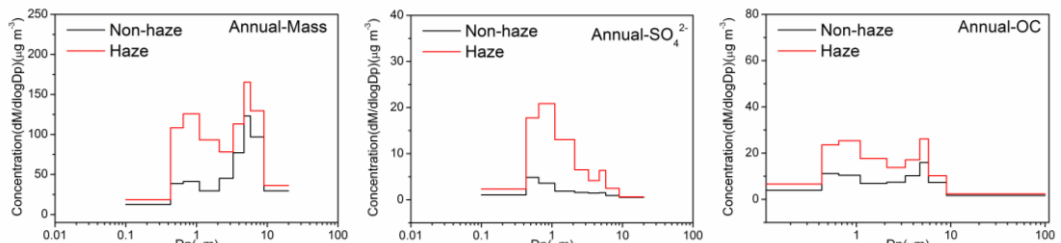
1160

1161 Fig. 2 Size-resolved mass concentration (distributions that are marked as solid circle  
1162 and open triangle denote haze and non-haze days, respectively).

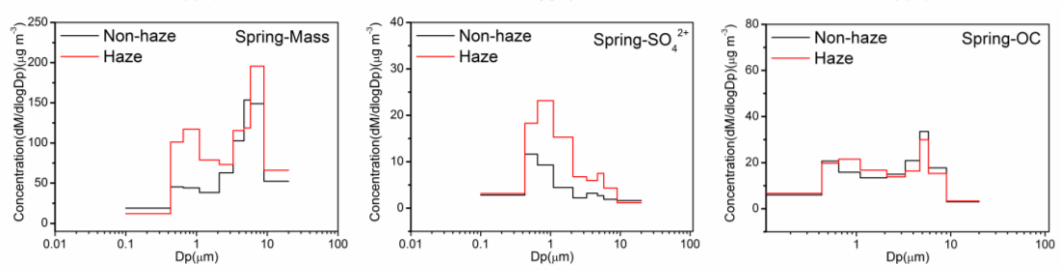
1163



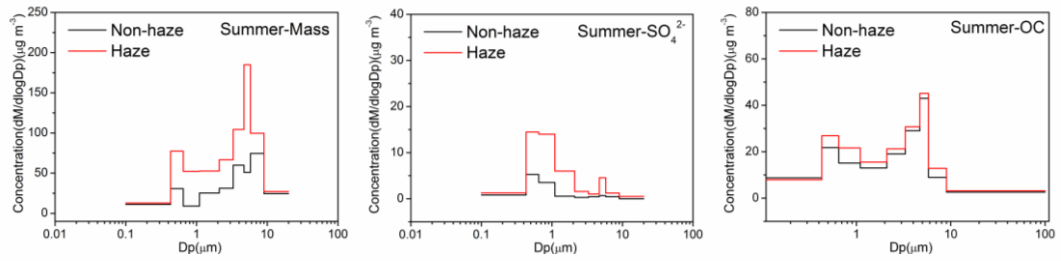
1164



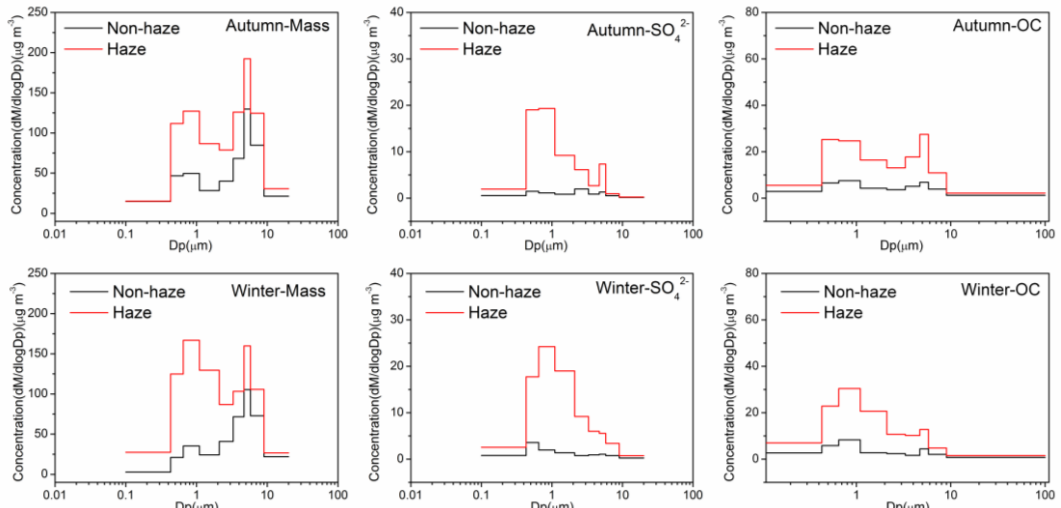
1165



1166

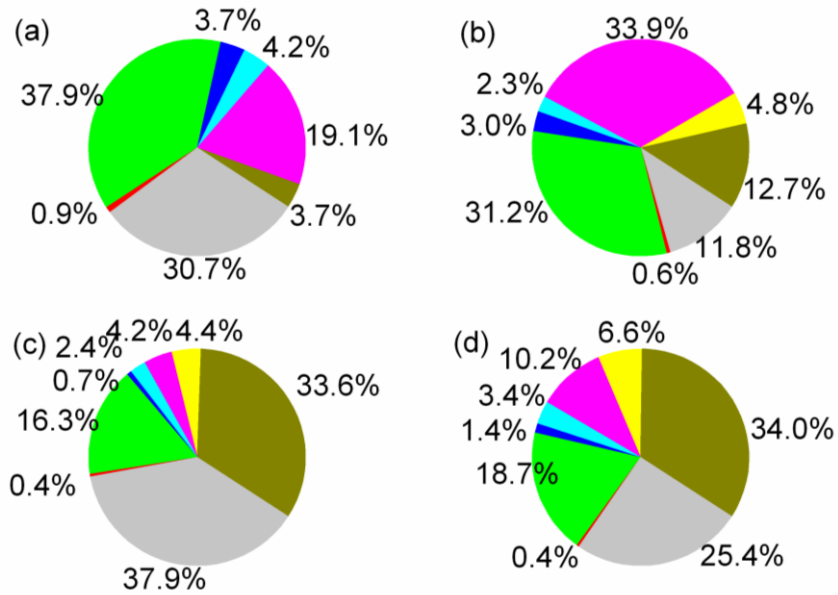


1167

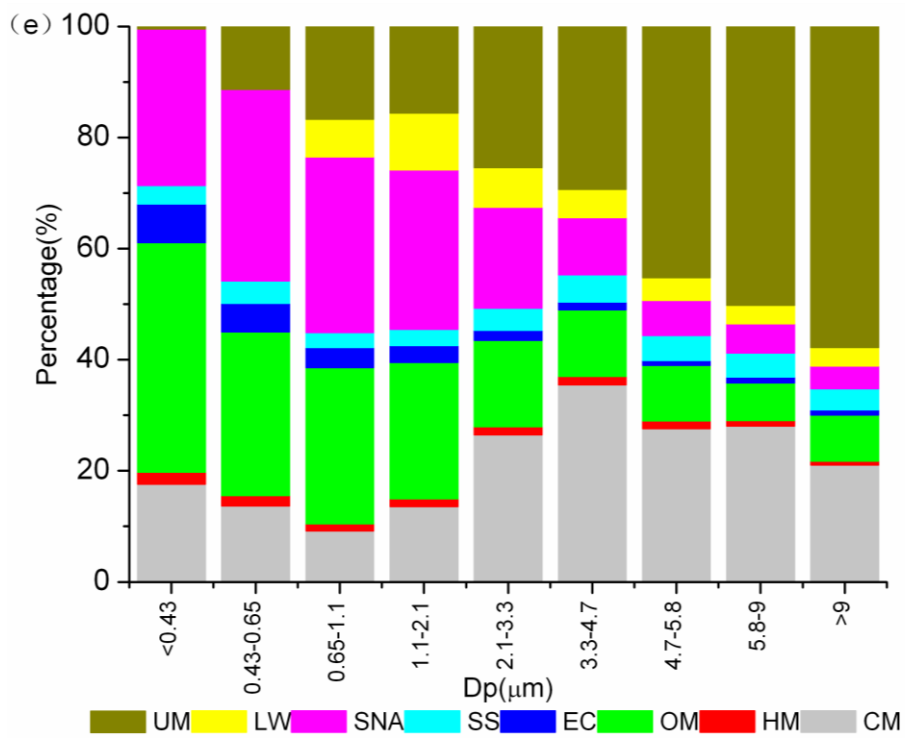


1168

1169 Fig. 3 Mass concentration size distributions on haze and non-haze days over the entire  
 1170 sampling period (annual) and by season as well as that of the typical chemical species.  
 1171



1172

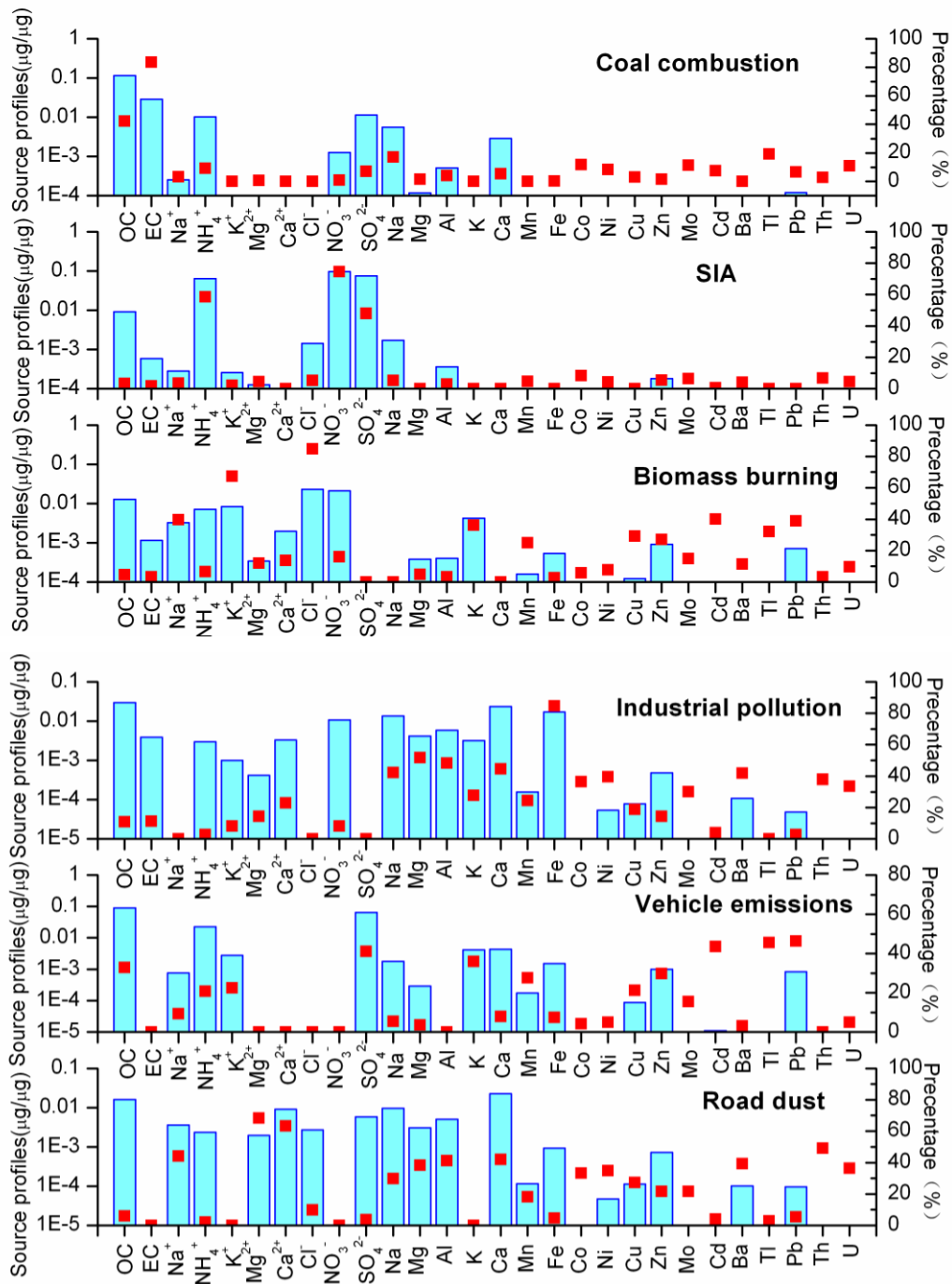


1173

1174 Fig. 4 Contributions of different components to the total masses in (a) PM<sub>2.1</sub> on  
 1175 non-haze days; (b) PM<sub>2.1</sub> on haze days; (c) PM<sub>2.1-9</sub> on non-haze days; (d) PM<sub>2.1-9</sub> on  
 1176 haze days; (e) different size fractions.

1177

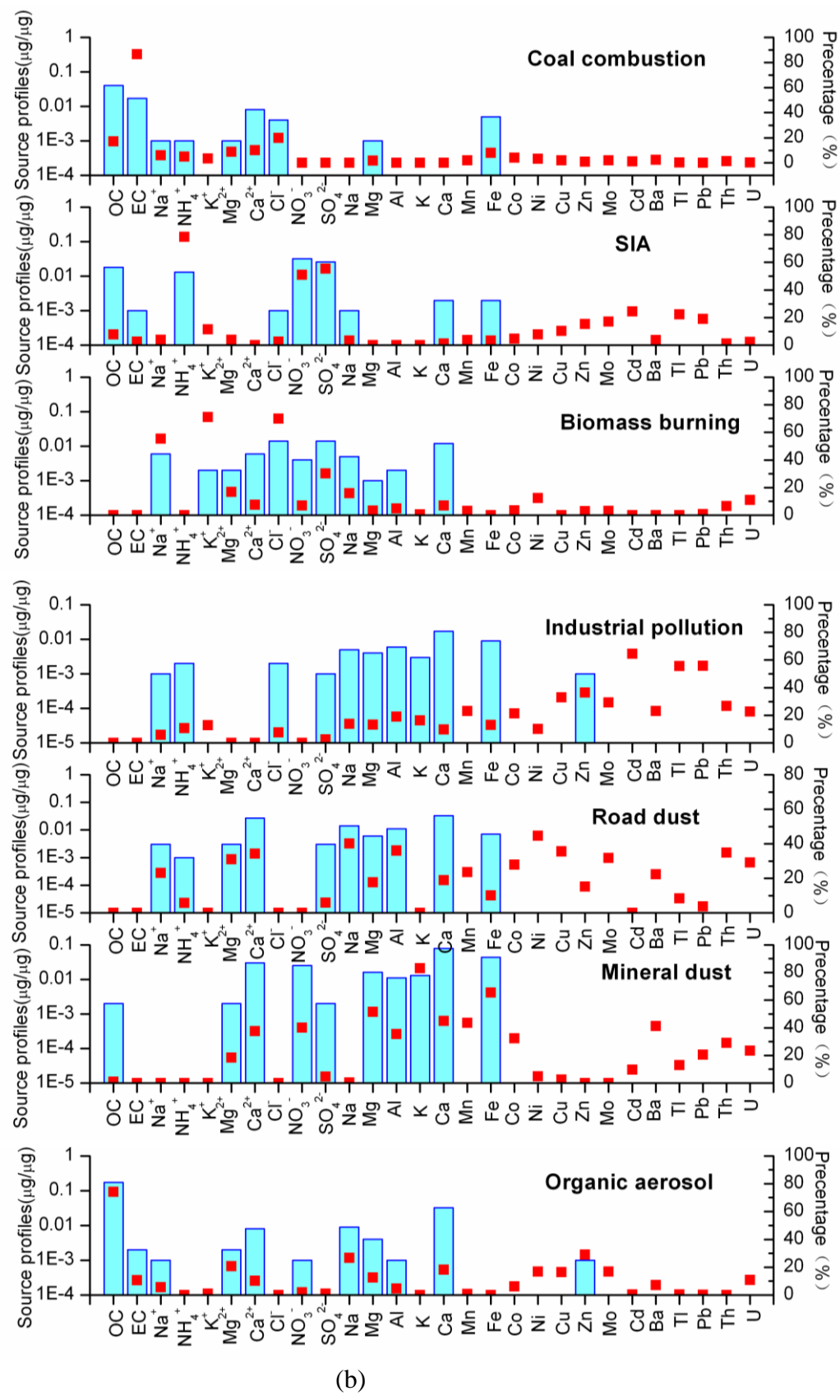
1178



1179  
1180

(a)

1181

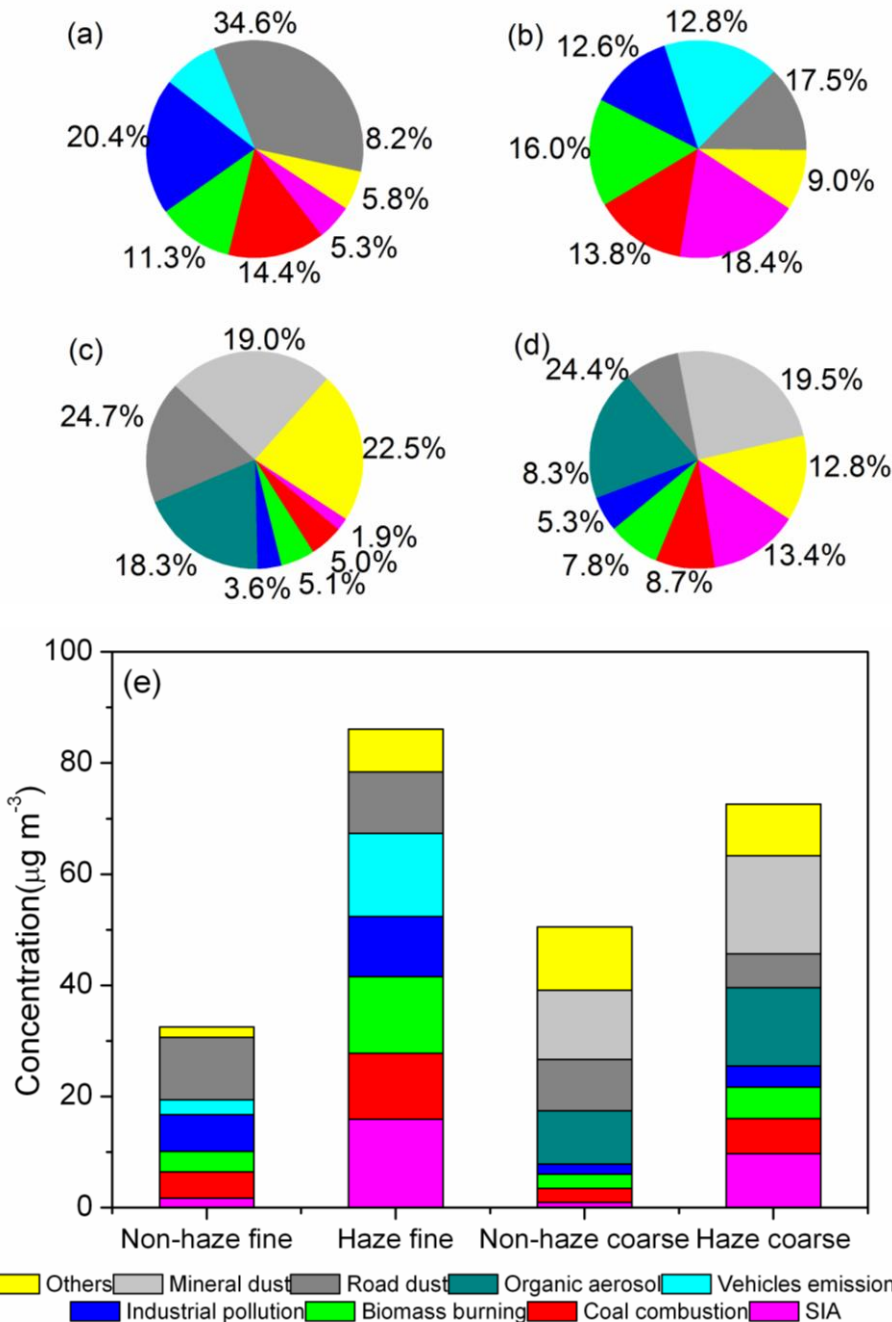


(b)

1185 Fig. 5 The profiles of each source in (a) fine and (b) coarse fractions.

1186

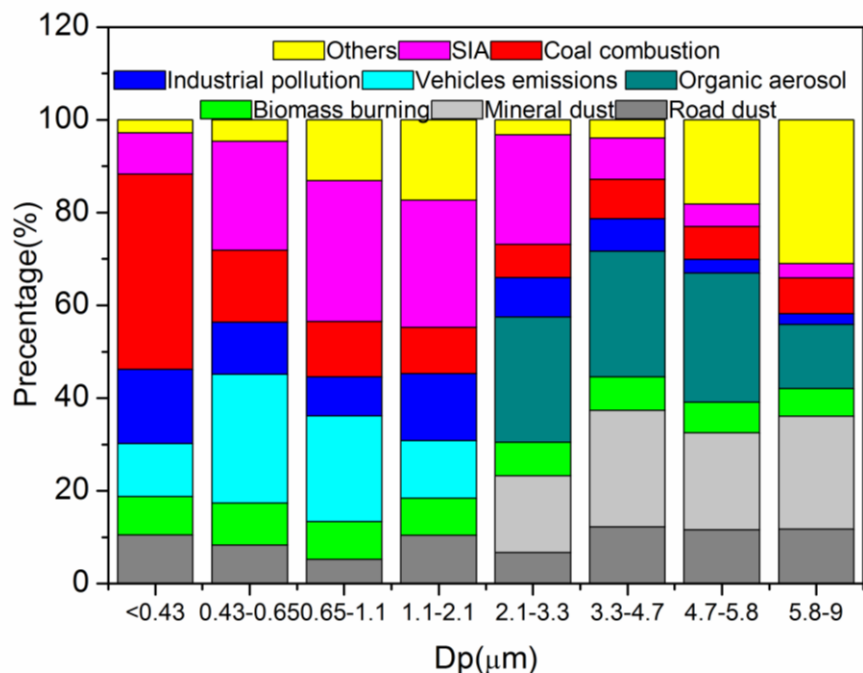
1187



1188

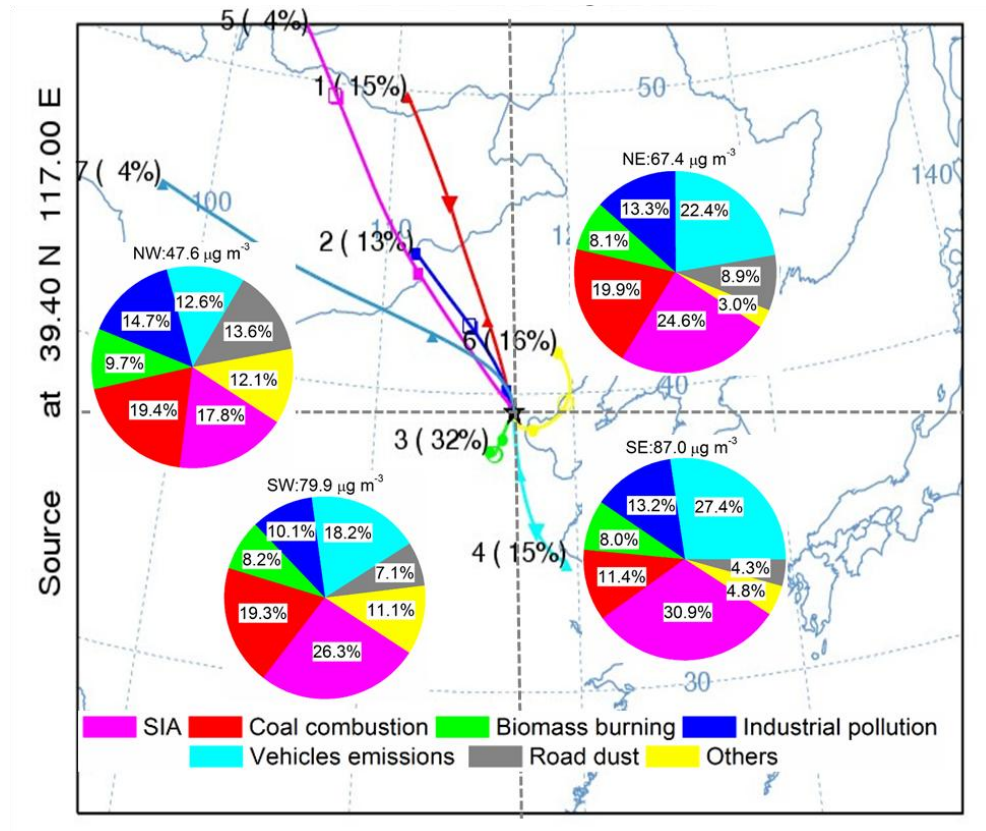
1189 Fig. 6 Relative contributions from each identified source to (a) PM<sub>2.1</sub> on non-haze  
 1190 days; (b) PM<sub>2.1</sub> on haze days; (c) PM<sub>2.1-9</sub> on non-haze days; (d) PM<sub>2.1-9</sub> on haze days  
 1191 and (e) mass concentrations of each source.

1192



1193

1194 Fig. 7 Relative contributions from each identified source to different size fractions.  
1195



1196

1197 Fig. 8 Relative contributions from each identified source to PM<sub>2.1</sub> at different  
1198 trajectory clusters.

1199 Table 1 Concentrations of different chemical compositions in size-resolved particles during entire sampling period (annual) and four seasons ( $\mu\text{g}$   
1200  $\text{m}^{-3}$ ).

Ni	0.013	0.014	0.011	0.012	0.014	0.010	0.014	0.018	0.014	0.015
Cu	0.026	0.020	0.030	0.020	0.015	0.015	0.029	0.022	0.029	0.023
Zn	0.21	0.10	0.24	0.12	0.18	0.09	0.23	0.09	0.19	0.09
Mo	0.006	0.006	0.002	0.001	0.002	0.002	0.002	0.001	0.002	0.002
Cd	0.001	0.000	0.001	0.000	0.001	0.000	0.001	0.000	0.001	0.000
Ba	0.017	0.043	0.018	0.057	0.014	0.032	0.018	0.044	0.017	0.039
Tl	0.001	0.000	0.001	0.000	0.001	0.000	0.001	0.000	0.001	0.000
Pb	0.089	0.018	0.094	0.022	0.071	0.013	0.088	0.015	0.103	0.022
Th	0.000	0.000	0.000	0.001	0.000	0.000	0.000	0.000	0.000	0.001
U	0.000	0.000	0.000	0.000	0.000	0.000	0.000	0.000	0.000	0.000

1201

1202

1203